

X-ray Computed Tomography

Philip J. Withers¹, Charles Bouman², Simone Carmignato³, Veerle Cnudde^{4,5}, David Grimaldi⁶, Charlotte K. Hagen⁷, Eric Maire⁸, Marena Manley⁹, Anton du Plessis¹⁰, Stuart R. Stock¹¹.

P.J. Withers is the corresponding author:p.j.withers@manchester.ac.uk

1. Henry Royce Institute, Dept of Materials, University of Manchester, Manchester M13 9PL, UK

2. School of Electrical and Computer Engineering, Purdue University 465 Northwestern Avenue, West Lafayette IN USA

3. Department of Management and Engineering, University of Padova, Stradella San Nicola 3, Vicenza, Italy

4. Pore-Scale Processes in Geomaterials Research (PProGRess) – UGCT, Department of Geology, Ghent University, Krijgslaan 281/S8, Ghent, Belgium

5. Environmental Hydrogeology, Department of Earth Sciences, Utrecht University, Princetonlaan 8a, CB Utrecht, The Netherlands

6. Division of Invertebrate Zoology, Professor, Gilder Graduate School, American Museum of Natural History, Central Park West at 79th St., New York, New York USA

7. Department of Medical Physics and Biomedical Engineering, University College London, London WC1E 6BT, United Kingdom

8. Universite de Lyon, INSA-Lyon, MATEIS, CNRS UMR5510, Villeurbanne, France

9. Department of Food Science, Faculty of AgriSciences, Stellenbosch University, Private Bag X1, Matieland (Stellenbosch), South Africa

10. Research Group 3DIInnovation, Stellenbosch University, Stellenbosch, South Africa

11. Dept. of Cell and Developmental Biology, Feinberg School of Medicine, Northwestern University, Chicago IL USA.

Abstract

X-ray computed tomography (CT) can reveal the internal details of objects in three dimensions (3D) non-destructively. We outline the basic principles of CT and describe the ways in which a CT scan can be acquired using X-ray tubes and synchrotron sources including the different possible contrast modes that can be exploited. We explain the process of computationally reconstructing 3D images from 2D radiographs, and how to segment the 3D images for subsequent visualisation and

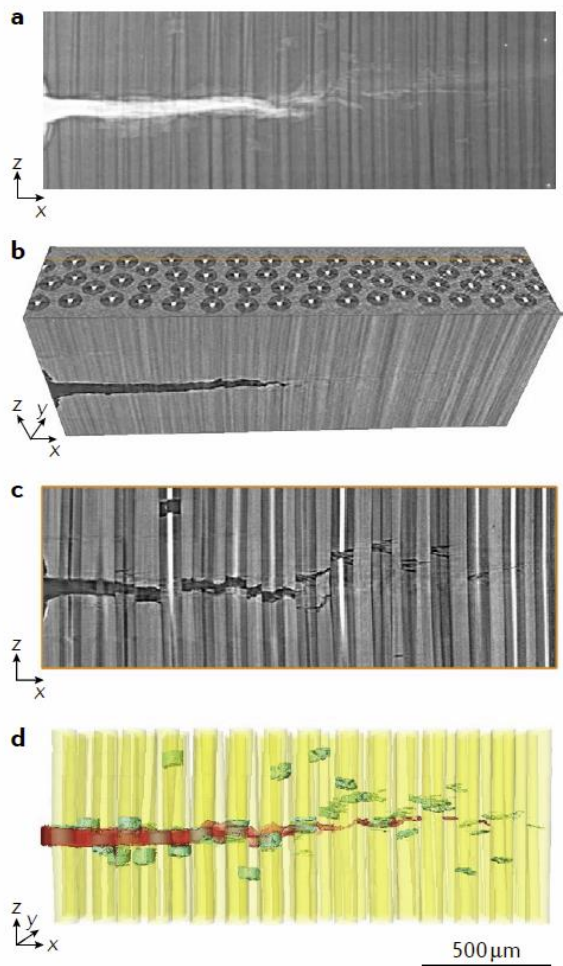
quantification. While CT is widely used in medical and heavy industrial contexts at relatively low resolutions, here we focus on the application of higher resolution X-ray CT across science and engineering. We consider the application of X-ray CT to study subjects across the materials, metrology and manufacturing, engineering, food, biological, geological and paleontological sciences. We examine how CT can be used to follow the structural evolution of materials in 3D in real time, or in a time-lapse manner, for example to follow materials manufacturing or the in-service behaviour and degradation of manufactured components. Finally, we consider the potential for radiation damage and common sources of imaging artifacts, discuss reproducibility issues, and consider future advances and opportunities.

[H1] Introduction

X-ray computed tomography (CT) can provide unrivalled information about the internal structure of materials non-destructively from the metre down to the tens of nanometre length scales. It exploits the penetrating power of X-rays to obtain a series of two dimensional (2D) **radiographs** [G] of the object viewed from many different directions. This process is sometimes called a CT scan. A computed reconstruction algorithm is then used to create a stack of cross-sectional slices from these 2D **projections** [G] (radiographs) of the object. As illustrated in Box 1, this process provides a digital 3D **greyscale** [G] representation (often referred to as a **tomogram** [G]) of the internal structure of the object. This can be quantitatively analysed, virtually sliced in any direction, or specific constituents can be digitally colour-coded, or rendered transparent, to visualise the 3D morphology.

One of the main advantages of imaging by X-ray CT over other techniques is that it is non-destructive. This is critical when examining delicate samples which cannot easily be sectioned (for example frozen ice cream ¹), or those which should not be damaged (for example cultural artefacts ²), or where the structural integrity of an engineering component must be assured before it is deployed (such as a turbine blade). This, and the fact that modern CT systems can operate at X-ray doses that pose a relatively low risk to human health ³, has led to its widespread use as a medical diagnostic tool. The non-destructive aspect also opens up the

Different types of X-ray CT images



Box 1: Synchrotron CT scan of a fatigue crack in a titanium/silicon carbide tungsten-cored monofilamentary fibre metal matrix composite imaged at maximum crack opening load. a) Radiograph (projection); b) reconstructed tomogram; c) virtual cross-section; d) volume rendering showing fibres (yellow), titanium matrix (transparent), matrix crack (red), fibre fractures (green). (Courtesy Y. Wang, T.L. Burnett, P.J. Withers)

possibility of longitudinal studies monitoring the evolution of 3D structure, for example the growth of a malignant tumour undergoing treatment ⁴, or the manufacture and assembly of products ⁵, or their degradation in service ⁶. In this respect, CT scanning can either be undertaken periodically in a time-lapse manner, such as to follow the metamorphosis of a chrysalis ⁷, or continuously in real time, such as to track the progress of a fluid through rock ⁸, or cracks during the fracture of a sample ⁹, or the catastrophic thermal runaway failure of a lithium battery ¹⁰.

The contrast recorded by each projection is dependent on the interaction of X-rays with matter. As a result, several contrast modes are possible which suit different types of imaging task. When an electromagnetic X-ray wave passes through an object, both the intensity and the phase change vary according to the refractive index, n:

$$n=1 - \delta + i\beta \quad (1)$$

where the imaginary part (β) controls the attenuation (absorption) and the real part (δ) the phase shift as the X-rays pass through the object. The former is exploited to obtain **attenuation contrast** [G], the latter is exploited for **phase contrast** [G]. The **linear attenuation coefficient** [G], μ , expresses the attenuation of X-rays as they pass through the material and is given by $4\pi\beta/\lambda$ where λ is the X-ray wavelength¹¹.

When deciding whether, or how, to undertake a CT scan several important factors need to be considered, including the object size, the features of interest and their composition, the allowable dose and the **temporal resolution** [G]. Just as 2D images are made up of 2D **pixels** [G], 3D images are made up of many cubic volume elements called **voxels** [G]. The **spatial resolution** [G] is typically considerably larger than the voxel size, depending on the scanning conditions⁵. While one can detect features that are smaller than the voxel size if they are reasonably well separated and have sufficient contrast to differentiate them from noise in the reconstruction, to properly characterise features (shape, volume, etc) the selected voxel size must be significantly smaller than size of the expected features or their separation. Conventional (medical or heavy industrial) CT generally refers to sub-millimetre resolutions or poorer (voxel sizes $\geq 100 \mu\text{m}$), microtomography (microCT) to micrometre resolutions (voxel sizes $\geq 0.1 \mu\text{m}$), and nanotomography (nanoCT) to nanometre resolutions (down to $\sim 10 \text{ nm}$ voxels). Selecting a smaller voxel size usually means accepting a smaller object size. This is in part because having a smaller effective pixel size generally means recording a smaller field of view (FoV) on the detector. But it is also because of the increase in acquisition time associated with stitching together multiple fields of view, along with the marked increase in the computational reconstruction task and the storage requirements, as the sample/voxel size ratio increases.

In addition to selecting a scanner with the appropriate spatial resolution, the contrast between features is critical to their detection. Indeed, **contrast agents** [G] and phase contrast can be used to detect details finer than the spatial resolution. Since the linear attenuation coefficient generally rises sharply with increasing atomic number (due to scattering by the electrons) and falls with increasing X-ray energy, attenuation contrast is well-suited to distinguishing materials with large differences in electron density, for example bone fractures (contrast between calcium containing hydroxyapatite and cracks) and porous networks in hydrocarbon reservoirs (contrast between sandstones or carbonates and pores). Low atomic number materials, such as soft tissue and carbon fibre composites, generally show poor attenuation contrast, and are better suited to phase contrast

imaging. For the imaging of intracellular detail, soft nanoCT can exploit the water window (energies between 284 eV and 543 eV) across which water is essentially transparent. The attenuation contrast can be tailored by selecting the X-ray energy (**monochromatic beam [G]**) or range of energies (**polychromatic beam [G]**) used. Too high an energy can lead to low attenuation and hence poor contrast, while too low an energy can lead to no penetration and hence little detected signal. This balance between contrast and sample penetration means that as the sample size increases the optimal X-ray energy increases. As a result, nanoCT systems usually work at either soft (<1keV) or moderate energies (5–30keV), microCT and clinical scanners at high energies (30–300keV and 80–140keV respectively), and heavy industrial CT systems at very high energies (>400keV).

The field of X-ray computed tomography is expanding rapidly both in terms of the range of applications and with regard to the development of new imaging modalities. In this Primer, we focus on introducing the general principles underlying conventional scalar attenuation and phase contrast CT, and their practical implementation and limitations across a range of applications in the area of micro- and nanoCT. For the application of CT imaging within a clinical context the reader is referred to ^{4,12} and to ⁵ with regard to high energy industrial CT. Similarly the reader is pointed elsewhere for a discussion of advanced methods^{13–15}, for example where scattered signals (such as diffraction, fluorescence, etc.) are used to reconstruct the spatial variation of tensor properties (for example strain ¹⁶, polycrystalline grain orientations ^{17,18}, crystalline phases ¹⁹, nanostructure ²⁰ or elemental composition ²¹).

[H1] Experimentation

In this section we introduce the principal components of CT scanners and their typical configurations before considering attenuation and phase contrast CT.

[H2] Experimental configuration

The three basic physical components of a CT scanner are the X-ray source, the X-ray detector and the sample stage (FIG. 1). The architectural principle “Form follows function” ²² also governs CT system design and use. Function can be viewed from two inter-related, but somewhat different perspectives: one dictated by the objects being imaged, and the other defined by the nature of the X-ray source and detector.

If the function is patient or laboratory animal imaging, for example, then the form is determined by the need for the patient and their organs to remain motionless. Therefore, the form is: a scanner located in the clinic or laboratory, where the X-ray source and detector rotate around the supine “patient” (FIG. 1a). If the function is to image centimetre- or millimetre-sized specimens, then the X-ray source and detector are best kept stationary while the specimen rotates (FIG. 1 b and FIG. 1 c).

From the perspective of instrument function, the X-ray source and X-ray detector dictate practical scanner forms. In most cases, the source is either an **X-ray tube [G]** or a **synchrotron [G]** storage ring. In both cases, X-rays are produced by the acceleration of electrons. X-ray tubes are (relatively) simple, numerous and inexpensive devices that power laboratory CT scanners, whereas there are relatively few synchrotron facilities world-wide, each hosting dozens of experimental stations (including CT beamlines) tangential to the storage ring. Their beams differ in terms of **X-ray flux [G]**, source size and X-ray energy spectrum, as discussed below and in detail elsewhere ²³.

Tube sources emit a wide spectrum of X-ray energies (a broad polychromatic — usually white — beam along with sharp peaks characteristic of the target material) in a cone. The maximum energy of this spectrum of X-ray energies is determined by the electron [accelerating voltage \[G\]](#). To use as many photons as possible that emanate from the source, tube source microCT instruments typically use the cone beam design (FIG. 1b). The solid angle of the X-ray cone illuminates a significant sample volume. The geometrical magnification of the image can be increased by moving smaller samples closer to the source (and farther from the detector), so as to expand the projection of the image across more pixels on the detector. This geometrical magnification decreases the effective size represented by each voxel. Scan times typically range from minutes to hours depending on the resolution required.

In a synchrotron, the path of circulating electrons is bent and accelerated radially either by [bending magnets \[G\]](#) or by [insertion devices \[G\]](#) such as undulators or wigglers²³. The resulting highly directional X-ray beam travels down a vacuum beam pipe to the experiment (here the tomography station). Synchrotrons provide many orders of magnitude more flux than tube sources and often a monochromatic beam is selected from the X-ray spectrum. This improves sensitivity to small differences in absorptivity and limits certain artifacts. Often the beam is spatially coherent, an advantage for imaging with phase contrast (see below). The X-ray beam reaching the specimen is typically highly parallel (FIG. 1c) because the X-ray source is tens to hundreds of meters from the object. As a result, the reconstructed voxel size is equal to the detector pixel size. Scan times typically range from sub-second to minutes²⁴.

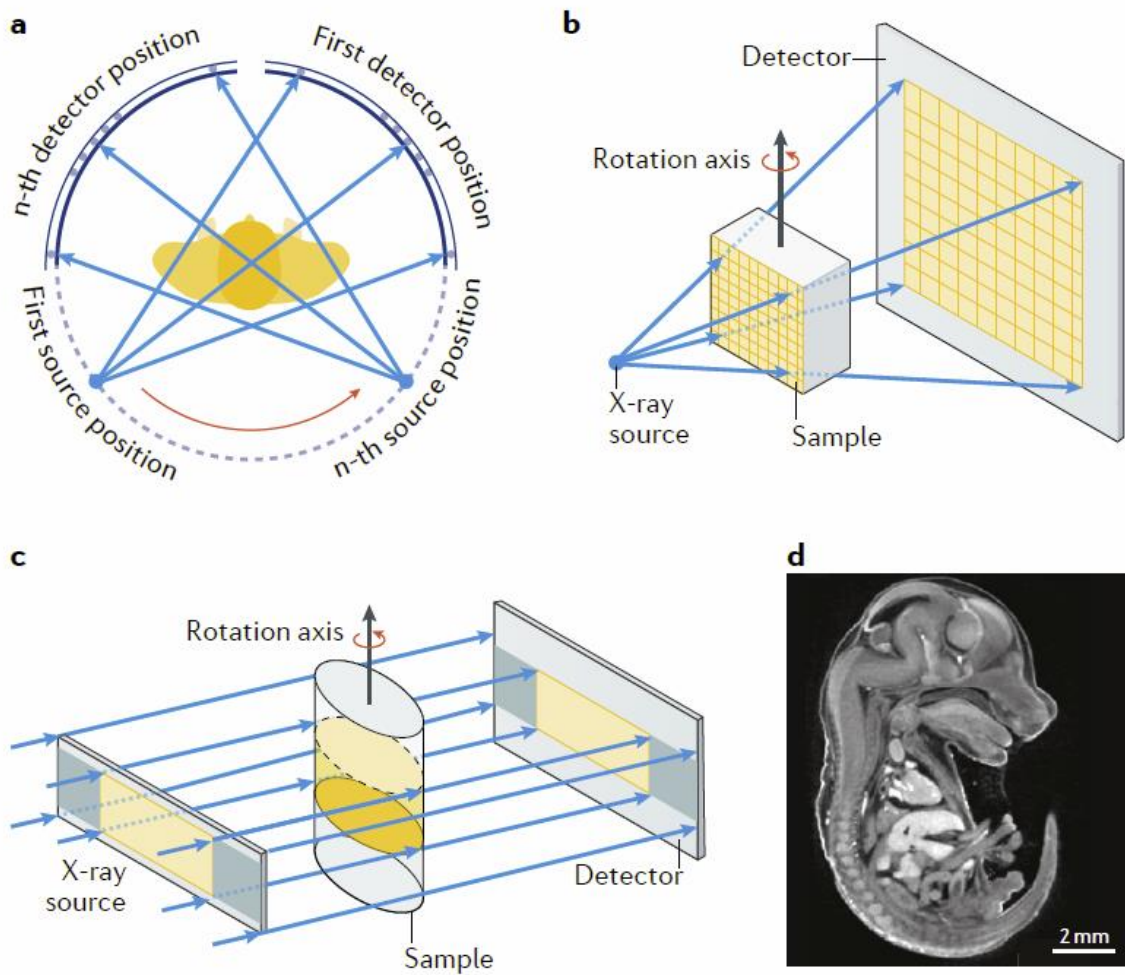


Figure 1. Common X-ray CT configurations. a) gantry system where the source and detector rotate in tandem around the patient, animal or specimen; b) Cone beam system typical of laboratory systems ²⁵; c) parallel beam system geometry typical of synchrotron X-ray systems ²⁵; d) a virtual slice through an attenuation contrast tomogram of an iodine-stained mouse embryo ²⁶.

Strict adherence to the mathematical assumptions underlying reconstruction algorithms dictates that the entire sample cross-section should be fully illuminated and remain within the FoV of the detector for all projections. It is common practice to select a magnification ratio (cone beam), or beam size (parallel beam), that ensures the full width of the sample lies within the FoV (although this need not necessarily be the case for every scan). The systems shown in FIG. 1 are projection systems having no lenses; in contrast, nanoCT instruments often employ X-ray condenser and objective lenses (for example, zone plates) in arrangements like that shown in FIG. 2a. In such cases, voxel sizes less than 50 nm can be used for specimens having dimensions \sim 50 μ m or less ²⁷.

X-ray area detectors are normally used to record the spatial pattern of transmitted X-ray intensities across each projection. Most detectors convert X-rays to visible light with a scintillator and then, via an array of complementary metal-oxide semiconductor (CMOS) or other devices, to electrons for digital processing. In laboratory microCT, where it is critical to capture as many X-ray photons as possible, designers most often couple the scintillator and CMOS array by affixing them to opposite

sides of a fibre optic array. In synchrotron microCT, where photon flux is high, less efficient and low depth of focus optical lenses often link single crystal scintillators with CMOS detectors, which allows resolution well below the detector pixel size. Because the illumination provided by X-ray sources is far from uniform, and detectors show pixel to pixel variations in sensitivity, a projection must be acquired without the sample in the FoV to compensate for these variations during reconstruction: this is called a **flat field correction** [G].

Mechanical stability (both of the instrument and the specimen) is essential in tomography. The precision/accuracy of motions must be smaller than the voxel size otherwise features within the reconstruction will be blurred. While prior calibration can correct known (i.e. reproducible) inaccuracies, wobble of the rotation axis or movement of the X-ray source during a scan, for example, can seriously degrade reconstructions. Adequate warmup of the X-ray tube (laboratory) or monochromator (synchrotron) is also important to avoid blurring due to thermally-induced movement of the source during a scan.

Alternative tomographic arrangements can be extremely valuable for certain applications. For example, large aspect ratio panels and circuit boards present a serious challenge for conventional CT because of the inability to collect signals over the full 180° rotation. In such cases **laminography** [G]²⁸ can be used; it is a tomographic method using planar translation of specimen and detector coupled so that all features outside of the selected focal plane are blurred out.

[H2] Attenuation Contrast CT

The contrast obtained in each projection of the object is related to the attenuation of the beam. It is given by the line integral of the attenuation arising from the material encountered on the path of the beam as it passes through the object. For an object comprising multiple ($i=1$ to n) materials in the beam path, the transmitted intensity, I , falls exponentially compared to the incident intensity, I_0 , and is described by Beer-Lambert's Law;

$$I = I_0 e^{-\sum_i^n \mu_i x_i} \quad (2)$$

where μ_i and x_i are the linear attenuation coefficient of, and path length through, the material, i . Each reconstructed slice is a map of the linear attenuation coefficient $\mu(x,y,z)$ for the corresponding section in the object (see for example FIG 1d). Contrast sensitivity, which is the extent to which small changes $\Delta\mu$ can be detected, and resolving power, which is the degree to which small, closely spaced features can be distinguished, depend on the CT instrument, the sample and the data acquisition parameters. Materials having similar atomic numbers (Z) tend to produce little absorption contrast.

The signal to noise ratio within each radiograph affects the quality of the reconstruction. In terms of signal, differentiation of Eq. 2 reveals that optimum contrast is obtained for $\mu t \sim 2$ (14% transmissivity)²⁹. In practice, not all the photon paths can satisfy this criterion; one typically ensures that the transmissivity is never much worse than this by adjusting the X-ray tube accelerating voltage or the monochromatic energy. Note that avoiding detector saturation is also critical because this invalidates the flat field correction.

As mentioned in the introduction, the linear attenuation coefficient (μ) of a given element changes with X-ray energy; this variation is smooth except for step changes that occur at the characteristic **absorption edges** [G]. Since μ changes abruptly at the element-specific energies corresponding to

these edges, they can be used to enhance contrast in X-ray CT, or to identify the presence of different elements. In tube source CT, two scans are undertaken using different accelerating voltages in an approach termed dual energy CT (for an example, see³⁰). In synchrotron source CT, one can optimize contrast from element Z by collecting projection sets at energies on either side of a characteristic absorption edge of Z²⁹. In both cases, numerical comparison of the pairs of reconstructions shows where element Z is concentrated.

[H2] Phase contrast imaging

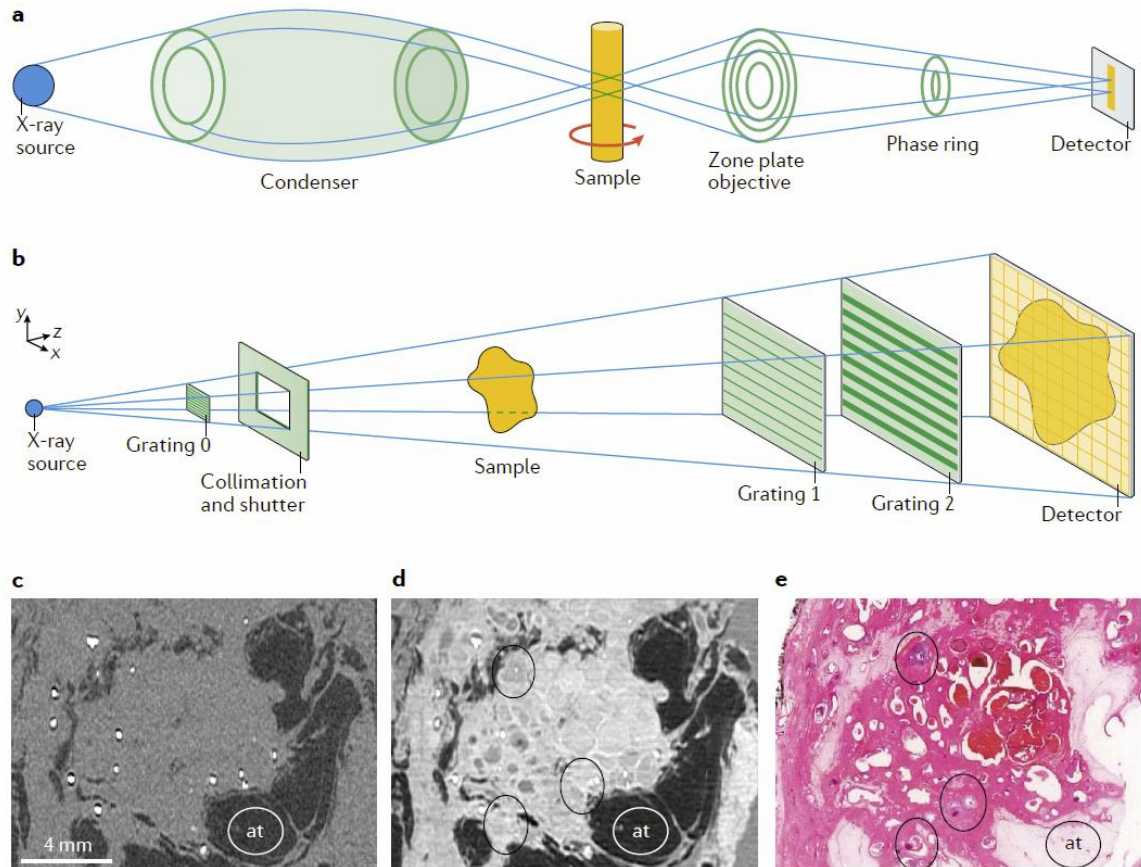


Figure 2. Phase contrast CT. a) Experimental setup for Zernike X-ray phase contrast, b) experimental setup for grating interferometry, c) attenuation and d) phase contrast CT images of breast tissue acquired with grating interferometry alongside e) the corresponding histological slice. AT denotes adipose tissue. Images taken from³¹.

While attenuation contrast suffices for visualising objects containing very different materials, many specimens contain materials that attenuate similarly (for example soft tissue), and better contrast can be obtained by exploiting the materials' X-ray phase contrast³²⁻³⁵ (FIG. 2). For example, an attenuation image of breast tissue (Fig 2c) reveals no differentiation of ductal structures and glandular tissue, although the microcalcifications are well-depicted. The corresponding phase-contrast image (Fig 2d), on the other hand, shows greater contrast with dilated ducts in the areas of ductal carcinoma (encircled regions).

Phase contrast stems from variations in the real part (δ) of the refractive index (Eqn 1), which generates a phase shift in the propagating X-ray wave front, rather than the imaginary part (β),

which describes the attenuation. For weakly-attenuating materials and within the lower X-ray energy regime, δ can be orders of magnitude larger than β ^{36,37}. As a result, greater contrast can be expected by designing the imaging process to detect phase shifts and by incorporating their extraction into the reconstruction step.

Phase shifts are detected indirectly by measuring modulated intensity patterns because direct measurement of the phase of an electromagnetic wave is difficult. Several different experimental approaches exist for detecting phase shifts. The simplest is propagation-based imaging (also called in-line phase contrast imaging)³⁸⁻⁴⁰, whose setup is identical to that of a conventional CT apparatus except that the detector is far from the sample instead of close to it. The X-ray wave passes through the specimen and propagates in space before its intensity is recorded; parts of the wave with different phases interfere, modulating the intensity and producing intensity peaks and troughs at internal and external boundaries. Certain reconstruction algorithms explicitly incorporate the pattern of boundary fringes into a map emphasizing differences in phase contrast. Propagation-based phase contrast microCT, where contrast increases with the distance between source and detector, is a standard option at many synchrotron beamlines³⁸.

Other X-ray phase contrast approaches rely on optical elements to convert phase shifts into modulated intensity patterns. Zernike phase contrast⁴¹⁻⁴⁵ is commonly implemented when spatial resolutions on the micrometre scale or below are required. Inserting a phase ring into the beam (FIG. 2a) generates a phase shift between the unscattered and scattered X-rays and increases the visibility of interference between them, which would otherwise be out of phase by approximately $\pi/2$. Other phase contrast imaging techniques can be grouped into interferometric and non-interferometric approaches. Grating interferometry⁴⁶⁻⁴⁸ is the most widely used interferometric method, where two (or three) finely pitched gratings facilitate indirect measurements of the phase shift (FIG. 2b). Non-interferometric methods are based on the idea that X-ray refraction — minute changes in the direction of travel — can be detected by means of a single crystal analyser and scanning across the crystal's diffraction peak (analyser-based imaging)^{49,50}, or by a beam stop array in front of the detector (edge illumination method)⁵¹.

In order to obtain high contrast images, the propagation-based and Zernike techniques should be implemented with spatially **coherent radiation** [G] either available at third generation synchrotrons or from micro-focus X-ray tube sources⁵². X-ray source technology has greatly advanced over the past decade and substantially increased the practicality of using phase contrast imaging in research laboratories outside large scale synchrotron facilities. Modern X-ray generators such as liquid metal jet sources⁵³, where a liquid rather than a solid target is bombarded with electrons, or inverse Compton sources⁵⁴, offer significantly higher flux at micron-scale focal spots than conventional X-ray tube technology and allow phase contrast scans to be performed within time frames suitable to living animals^{53,55}. In addition, grating interferometry and edge illumination techniques have relaxed source requirements and can be implemented in laboratory settings with non-micro-focal X-ray tube sources.

Irrespective of the approach and because detectors cannot measure phase, the phase shifts must be decoded from the recorded patterns of intensity: this process is known as phase retrieval. Numerous phase retrieval methods exist^{48,56-60}, varying in the complexity of the required input data. Paganin's method⁶¹ is most commonly used for propagation-based imaging. It assumes a constant linear

relationship between δ and β , allowing phase shift recovery by application of a low-pass filter to the intensity data.

[H1] Results

As the term computed tomography implies, the collection of the projection data is only the first step to obtaining a tomogram and deriving useful insights from it. Here we consider how computed reconstruction produces a 3D stack of slices from the 2D radiographs. Sometimes analysis requires only visual inspection of these (or other) virtual greyscale slices cut through the tomogram.

However, in many cases we need to quantify and 3D visualise specific regions within the volume.

This is achieved by **segmentation** [G], analysis and **volume rendering** [G] and this is outlined in the second half of this section.

[H2] Computed reconstruction methods

Computational reconstruction recovers the spatial distribution of the attenuation coefficient $\mu(x,y)$ (or phase decrement $\delta(x,y)$ for phase contrast) slice by slice, to form a greyscale image of the object, from the set of projections (radiographs). The relationship between the slices and projections is described mathematically by the **Radon Transform** [G]⁶². Two broad classes of reconstruction algorithms, namely analytic and iterative methods, are based on the transform.

For brevity, this section introduces the broad principles of the most commonly used analytic method, the filtered backprojection. The radiographs used in CT represent 2D projections of the specimen's attenuation according to Eqn. 2. By way of example, consider parallel beam CT (FIG. 1c) of an object (here a human head), as depicted in FIG. 3. If we consider one cross-sectional slice, as recorded by a row of pixels on the detector, we can represent the attenuation as a line profile. For a given projection angle, θ , each pixel on the detector sums the X-ray photons passing through the specimen slice along a given beam path; FIG. 3b shows three projection angles and the corresponding projection (a line profile) of absorptivity. As the sample is rotated, the row of pixels traces out a **sinogram** [G] (FIG. 3c) showing the variation in attenuation across the row of pixels as the projection angle varies. In FIG. 3d, the backprojection (BP) reconstruction algorithm⁶³ takes each projection making up the sinogram and mathematically projects it back along the angle θ at which they were recorded. In other words, the mass represented by each line profile is distributed uniformly along the ray path at each angle. This virtual mass builds up at positions where the intensity from different projections intersect. With increasing number of line profiles (corresponding to an increasing number of radiographs (projections)) backprojected, an increasingly faithful BP image of the object is recovered. It is evident from 3d that backprojection spreads mass where there is, in fact, no mass, introducing blurring into the reconstruction (as seen by comparing Fig 3a and Fig 3e). Filtered backprojection (FBP) corrects for this blurring by applying a filter (most commonly a ramp filter) to the projections. This suppresses the low frequencies to compensate for the high frequency components in Fourier space that are missing (due to insufficient sampling) and leads to a sharper image (Fig 3f)⁶⁴. More detailed mathematical treatments of this and other methods appear elsewhere⁶⁴⁻⁶⁶.

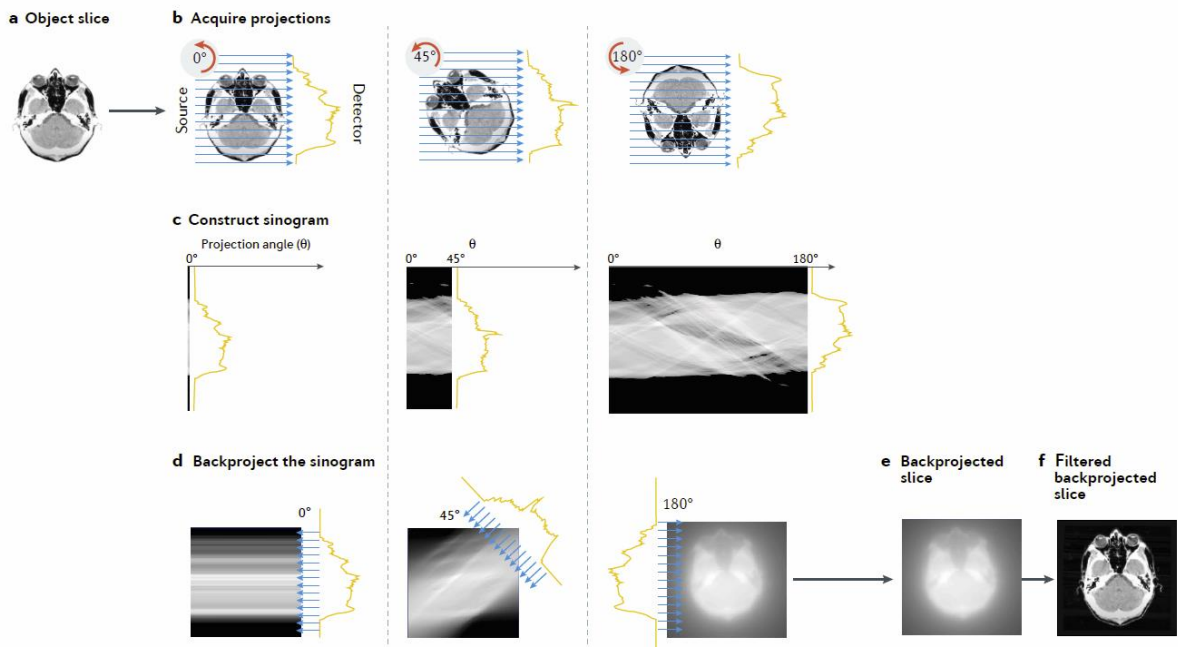


Figure 3. Schematic illustration of the backprojection reconstruction method for a single slice obtained by parallel beam CT. a) the original object slice (a human head where the highly attenuating features are brightest), b) a set of projections collected at different angles c) the sinogram resulting from many projections, d) the process of backprojecting the sinogram e) the final backprojected image, f) the equivalent filtered backprojection image. Note that with fewer projections, the image quality would decrease.

In parallel beam geometry (FIG. 1c), attenuation from each slice is independent of the other slices, and each slice in the stack can be reconstructed separately. In contrast, cone-beam CT and the related helical CT employ beams diverging from an X-ray tube source. For a vertical rotation axis, the voxels within a given physical slice of the object therefore project to a lower/higher detector position when they are farther/nearer to the X-ray source. This means that sets of rays contribute to more than one slice, and the absorption paths must be treated in 3D and not 2D. If the cone-angle is small, practical reconstruction is possible using the Feldkamp, Davis and Kress (FDK) filtered backprojection algorithm⁶⁷, but incurs cone beam distortions. An exact reconstruction for the helical trajectory is possible with the Katsevich algorithm⁶⁸.

An important question to ask is: how many projections are required to recover an acceptable image? At a minimum, the angular change between projections should be no greater than the voxel size at the outer diameter of the object. Therefore, the number of points needed along the circumference to satisfy the sampling condition is $q\pi$, where q is the number of pixels across the diameter of the object. Since each projection profile provides two points along this circumference, the minimum number of projections = $q\pi/2$ ⁶⁴, which is in line with more rigorous analyses⁶⁹⁻⁷¹. This means that for a 2000 pixel detector around 3200 projections are recommended. In practice, it is often sufficient to use considerably fewer projections, especially if features in the centre of the FoV are of interest. When the number of projections is too sparse or non-uniform, then imaging artifacts will occur.

Even when the theory says there is no exact solution or when the data are severely under-sampled, high quality reconstruction is still possible through the use of iterative reconstruction methods that

incorporate prior information. First, a forward projection of the estimate of the object is used to create artificial projection data. This is then compared to the measured projection data to compute a correction term. This correction term is then backprojected onto the volumetric object estimate, and the process is repeated iteratively. The process can start either with an empty image estimate or using prior information, such as a standard FBP reconstruction of the object ⁷². Iterative reconstruction methods offer the potential for high quality reconstruction when the data is very noisy and sparse, but this is at the cost of a higher computational burden. Model-based iterative reconstructions (MBIR) go beyond modelling the statistics of the detected photons and include modelling of the acquisition process (scattering, beam hardening etc.). They can generate high-quality reconstructions, even when the data is highly under-sampled. Iterative methods are being used increasingly in cases where imaging is sub-optimal, i.e., where only a limited angular range or number of projections can be acquired, or for where the dose must be limited or the acquisition time must be short ⁷³.

Machine learning methods are emerging for the reconstruction of tomographic data sets. For example in situations where high temporal resolution is required, which dictates shortened detector integration times and a decrease in the number of projections ⁷⁴, machine learning methods can produce much better reconstructions than conventional analytic or iterative methods. In the spatial realm, convolutional neural networks and training data sets can produce super-resolution results, for example in clinical CT where 3 mm-thick slices can be recovered from data sets containing 15 mm-thick slices ⁷⁵.

[H2] Visualisation and quantitative analysis

In principle the constituent materials can be mapped across a tomogram by comparing the precise μ values recorded for each voxel against those tabulated for different materials at that X-ray energy ⁷⁶. In practice this is not easy. Firstly, different materials can have similar attenuation coefficients. For example attenuation coefficients for aluminium and silicon carbide differ by 1%, making it difficult to distinguish the phases in an aluminium/silicon carbide composite ⁷⁷. Secondly, highly accurate determination of densities by microCT is challenging and requires the use of standards scanned under the same conditions as the unknown sample ⁷⁸. Nevertheless, precise measurements of μ are used to quantify bone mineral density ⁷⁹.

Quantifying morphological characteristics such as phase fractions, particles sizes and shapes, and pore networks, requires segmentation of the volume image into regions representing the constituent materials. FIG. 4 illustrates a simple, but widely employed, segmentation approach for an idealized elliptical specimen of a low absorption material (dark grey) containing an array of two higher attenuating phases (medium and light grey). The object can be grouped into regions based on ranges of voxel values (often referred to as greyscale levels). The choice of **greyscale thresholds [G]** is often made with reference to the image's greyscale **histogram [G]**. In the idealised case (FIG. 4) the object can easily be segmented into its four component materials because the final result is relatively insensitive to the bounding greyscale thresholds chosen in FIG. 4b.

In practice, reconstructions typically contain noise, i.e., apparently random variations in the voxel values. Visualization can be severely hampered if this noise is not removed prior to segmentation, and pre-processing with median or other filters are often employed for this purpose. As illustrated for a gravel filter-pack ⁸⁰ in FIG. 4, in addition to any noise in the image, the physics of radiograph

collection and artifacts from the reconstruction process lead to wide peaks in histograms associated with the constituent phases of real specimens, and this complicates the choice of where to set the segmentation limits. The **partial volume effect [G]** also broadens histogram peaks. Since the greyscale levels for the three regions overlap, their separation based simply on greyscale thresholds is inaccurate and very sensitive to the thresholds chosen as well as to any artifacts in the image.

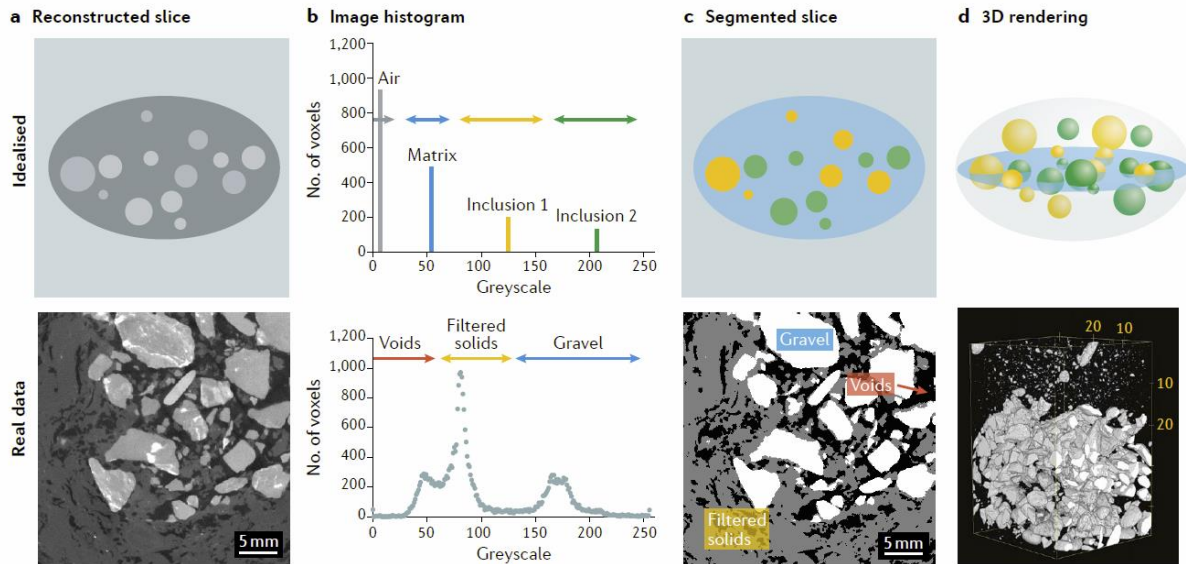


Figure 4. Illustration of the segmentation processes for an idealized sample (top) and a filter-pack for wetland water treatment⁸⁰ imaged by tube source microCT (bottom), both recorded as 8-bit images (a) in each case the reconstructed slice shows different phases according to the grey levels (b) greyscale histogram of the volume with the segmentation ranges used to segment the phases (c) segmented slice showing the segmented regions (d) 3D renderings of the segmented objects with the matrix phase rendered semi-transparent.

In addition to threshold-based methods, boundary-based and region-growing approaches are prominent^{23,81}. The features present and the type(s) of contrast dictate which method is preferable. If, for example, gradients of greyscale levels extend across the specimen due to uneven illumination from beam hardening, applying a global threshold is problematic, and a local threshold method, where a variable threshold is set relative to the voxel's neighbours⁸², works better. A powerful alternative is to segment based on a range of local greyscale gradients simultaneously with a range of greyscale levels⁸³. Boundary-based methods use relative differences in greyscale to detect the edges between materials. One example is mapping connected pore channels in a partially densified ceramic composite⁸⁴; the boundary following algorithm ignored isolated pores that global thresholding would have included. Watershed segmentation is a widely used region-growing method and is a direct analogue of the geographical or geological concept of a watershed: greyscale levels are considered heights and define different catchment basins. Watershed segmentation works well with foams where a significant fraction of cell walls cannot be detected⁸⁵. A rapidly developing alternative to conventional methods is machine learning/deep learning for segmentation, which is most developed in medical CT image analysis⁸⁶; typically a neural network is trained by the investigator, (where the investigator manually identifies regions representative of the constituent

phases) with the resulting neural network being capable of automatic segmentation of large image datasets.

Once segmented, many aspects of a tomogram can be quantified. Because X-ray CT can sample large volumes, it can provide excellent volume-averaged data or population distributions, including averaged quantities such as phase fractions (for example phase A and porosity in a matrix of phase B⁸⁷, or bone volume per total volume of tissue⁸⁸) or the surface area of phase A per unit volume⁸⁹. The large volumes that can be interrogated by CT make it ideal for locating and quantifying rare features or events that might be missed using cross-sectioning (for example in the case of manufacturing defects). For the dimensional quantification of features of interest, the measurement uncertainty must be kept under control and the voxels must be small enough that a number of them – depending on the application – span the smallest structural dimension of the feature; otherwise, partially filled voxels produce high sensitivity to segmentation parameters and concomitant bias. It is often difficult to decide whether small, segmented features are noise-related or real structures, and a common approach is to quantify only features exceeding a minimum number of contiguous voxels. This places a limit on the smallest features that can be identified as being a multiple of the voxel in size, depending on the application. It is sometimes useful to employ erosion/dilation operations (or the converse) to clean up segmented volumes. Erosion removes one voxel from each surface and dilation adds one voxel to each surface. If there are small, isolated pores within the segmented solid, applying dilation by a single voxel fills in the voids having a diameter of two voxels or fewer while adding a voxel to each external surface. By following this with erosion to the same degree the added surface voxels are removed but, because the internal voids no longer exist with the segmented solid, erosion does not reintroduce the small voids.

For microstructures which contain a network (for example plates and struts, blood or other vessels, pores, cracks) or an array of objects (particles, fibres, voids), examples of quantities of interest include mean feature dimensions or volumes, the associated standard deviation and the distribution (histogram) of the feature population. Note that thicknesses and lengths need to be measured in 3D: in 2D the apparent thickness of a plate depends on the angle that plate makes with the slice plane, and such potential bias of 2D sampling can invalidate any results. The distance transform method is widely used for valid, 3D thickness quantification⁹⁰ and is typically available in commercial packages such as BoneJ⁹¹ and other advanced software tools, especially for metrological applications (such FIG. 5a and Supplementary Video 3). The distribution of particle or void shapes can provide essential input for accurate modelling of structural evolution or fluid flow modelling. Connectivity of networks of struts and plates in structures (for example trabecular bone) can be a key determinant of mechanical integrity; permeability (related to the connectivity, pore throats [G] and tortuosity [G]) of porous networks can be critical to flow (of catalysts, or fluid through rocks – see FIG. 5i and supplementary video for example) while the distribution of particle contacts can determine kinetics of processing (for example in the case of sintering or granular flow). Examples of all these analyses appear in the literature across diverse fields (FIG. 5), such that even if a particular structural analysis is new in one field, something analogous may well have been quantified elsewhere.

The final step is often to visualise segmented images and many visualization approaches (and software packages) exist. Visualization can be as simple as displaying three orthogonal greyscale sections, or ortho-sections [G] (FIG. 5c), unwrapping a circular surface through the volume, or a virtual autopsy for cause of death determination⁹², or in forensic anthropology⁹³. More complex 2D

and 3D representations exploit colour, or render transparent, certain segmented phases (see examples in FIG. 4d and FIG. 5g), thereby highlighting important characteristics (see BOX 1). Any visualization interprets the data and should be viewed cautiously: small changes in the value of the segmentation threshold may highlight small gaps between features when the gap is actually noise, or they may merge closely spaced objects when there are real, but small, gaps. Fly-around videos or cut-throughs are increasingly common as a means of visualising the 3D nature of the object (see supplementary video 1 showing a Huntsman spider's head virtually extracted from amber) while structural alteration/evolution over time can be effectively demonstrated in time-lapse videos (supplementary video 2 of a chrysalis pupating). The impact of archived data can be further increased by observer-directed viewing or sectioning of 3D data sets (for example ⁹⁴), while augmented reality is becoming an increasingly important interactive tool in museums and elsewhere ⁹⁵.

[H1] Applications

X-ray CT can provide 3D and 4D (3D+time) information across a very wide range of applications. Here we do not hope to cover them all, but rather to illustrate the types of information, the most appropriate imaging modes and the insight that can be gained through a few chosen application areas.

In each example below, the researchers have had to identify the most appropriate imaging conditions. Firstly, they will have considered the resolution required; this is usually set to be about ten times the size of the smallest details to be observed in the sample. This determines whether a nanoCT or a microCT system is most appropriate, and what magnification is needed. This in turn dictates the field of view and whether region of interest scanning [G], or image stitching, are required to image a sufficiently large volume at the required resolution. The maximum pathlength through the sample then determines the maximum X-ray energy of the beam. For a given sample, this is a trade off because the lower the energy, the higher the attenuation contrast between the different phases inside the sample, but also, the lower the transmission. The energy is usually chosen to be the lowest energy that achieves enough transmission for all projections (say > 10–20 %). In some cases, a full 180° rotation may not be possible because of geometrical issues associated with extended laminar objects. If the attenuation contrast is unlikely to be sufficient to differentiate key features, phase contrast or sample staining can be considered. Finally, the scan time and dose required to obtain a scan of sufficient quality needs to be considered in terms of the exposure time and the number of projections. This is both because of the propensity for beam damage, but also for temporal studies where the frame rate needed to capture the events of interest is key. With regard to temporal resolution, synchrotron X-ray sources are able to provide a much higher X-ray flux than X-ray tube sources and so are especially well suited to high temporal resolution studies where thousands of projections can be acquired per second even at micron resolutions^{24,96}; X-ray tube source CT on the other hand is better suited to longer time-scale studies.

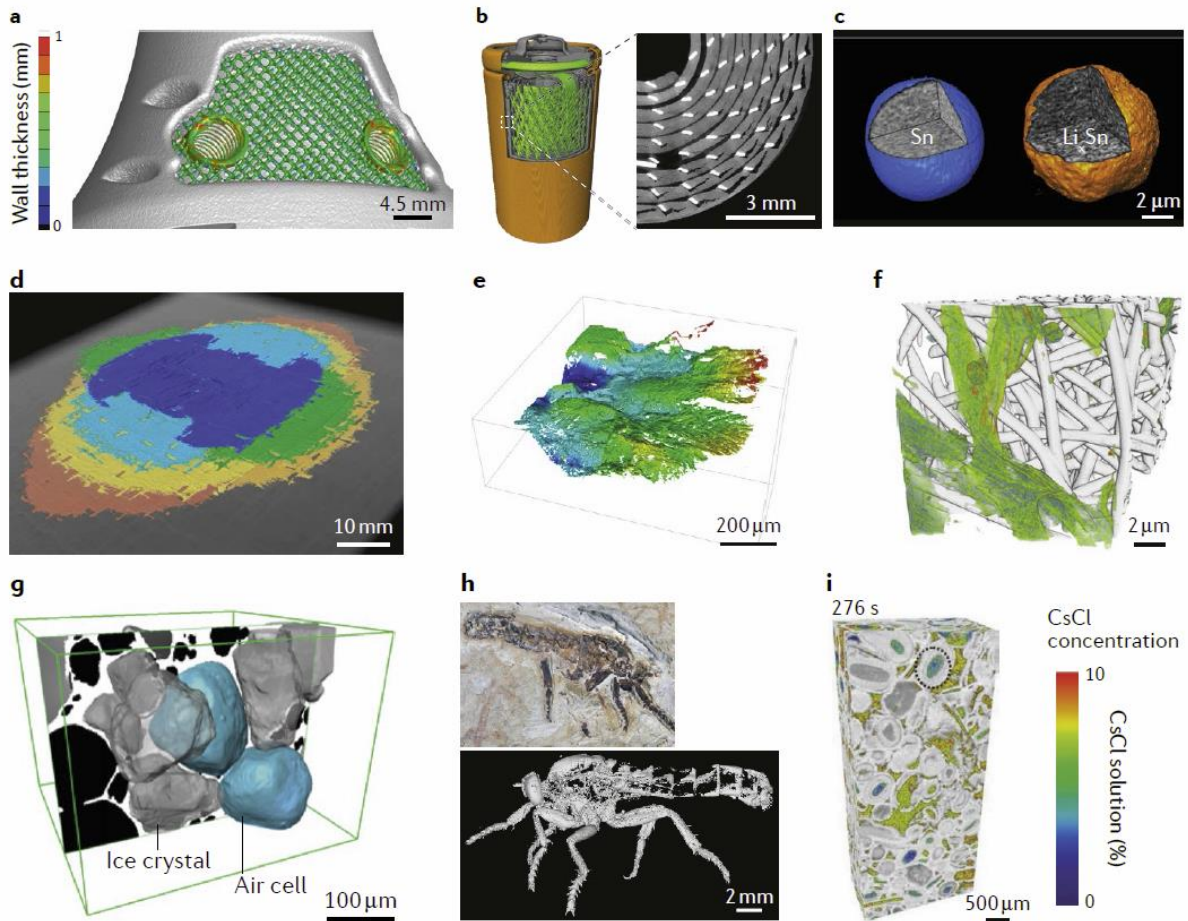


Figure 5: Examples of X-ray CT in different fields a) Industrial dimensional metrology of the lattice structure within an additively manufactured Ti alloy biomedical implant (tube source microCT, image courtesy du Plessis); the colour-coding shows that the local thickness of the lattice struts lie within an acceptable range (green ~ 0.5 mm). b) 3D rendering of a commercial Duracell CR2 battery showing the casing (orange), current collector mesh (green) connected via a tab to the terminal (green), and a manganese dioxide electrode (grey), inset showing cracks between electrode and current carrying mesh after discharge ⁹⁷ (synchrotron microCT). c) Evolution of surface morphology and internal microstructure of an individual tin particle in a lithium-ion battery electrode before and after the first lithiation (synchrotron nanoCT) ⁹⁸. d) 3D rendering of impact damage ply-by-ply for an 8-ply $[(0^\circ/90^\circ)2]s$ carbon fibre composite panel (tube source microCT) ⁹⁹. e) fatigue crack in an aluminium 2027 alloy where the crack length is 700 μm (synchrotron microCT) ⁹. f) 3D rendering of human fibroblast cells (green), with nuclei (red) distributed within an electrospun scaffold (grey) ¹⁰⁰ (tube source phase contrast enhanced nanoCT). g) Volume rendering during thermal cycling of ice cream showing the relationship between the air cells (blue) and the surrounding ice crystals (grey) (synchrotron microCT) ¹. h) a 115 million year old robber fly (Asilidae) from Brazil's Crato Formation preserved as iron hydroxide in a limestone matrix alongside a photomicrograph of the exposed portions (courtesy Hollister Herhold) (tube source micro CT). i) 3D rendering showing the infiltration of Savonnières limestone with caesium chloride after 276s. The dotted circle indicates an intragranular pore in which the flow is stagnant (Tube source microCT). ¹⁰¹.

[H2] Industrial metrology and manufacturing

X-ray CT is being used increasingly in manufacturing, not only to inspect and measure final products and components, but also to provide feedback in order to enhance quality at all stages of product development and manufacturing^{5,102}. The advantage of CT over conventional industrial metrology tools, such as coordinate measuring machines, is that CT is able to quantify internal features and details that are difficult/impossible to access externally¹⁰³. In addition to metrology, manufacturing defects such as pores, cracks, inclusions and density variations can be identified, providing quality assurance of the parts. The development of factory-style high-throughput in-line CT systems for rapid quality assurance inspections is now feasible¹⁰⁴.

CT has been used with great success in the automotive and aerospace industries, for example to inspect metal castings for porosity, and to inspect welds and joints for porosity, cracks and for bond quality^{105,106}. It is particularly advantageous in additive manufacturing, where some level of porosity tends to be unavoidable and its distribution can be very heterogeneous within complex 3D parts. CT images can guide manufacturing process optimisation, paying particular attention to critical defects such as clusters of pores, near-surface pores or irregular lack-of-fusion pores¹⁰⁷⁻¹⁰⁹. For highly engineered parts, the limitation is that the critical defect sizes can be small (for example, tens of micrometres), which means that only relatively small samples can be scanned at sufficient spatial resolution. However, representative small test samples can be scanned for manufacturing process development, or for regular process quality checks. X-ray CT is also being applied to composites manufacturing, where delaminations are particularly important¹¹⁰, as well as in the fabrication of batteries and fuel cells, where insights into internal structure can be related to degradation behaviour¹¹¹ (FIG. 5b). Other examples include the evaluation of manufacturing and assembly errors in electronic products, packaging materials such as polymer food packaging, glass bottles and enclosures and paint coating thickness distributions, to name but a few.

The ability of X-ray CT to follow processes in a time-lapse manner (BOX 2) is being used to increase the effectiveness of manufacturing processes. An example is observing the efficacy of hot isostatic pressing in closing porosity of additively manufactured parts by CT imaging before, and after, the processing step^{112,113}. Similarly, in-service parts can be subjected to CT at regular intervals to evaluate wear, fatigue crack formation, and growth or deformation of parts due to service use, and thereby evaluate their safe life potential¹¹⁴. All the above areas are still being developed and show great potential for CT in advanced manufacturing and engineering failure analysis.

Industrial metrological applications typically demand high dimensional accuracy and pose specific requirements that can be challenging for X-ray CT. Furthermore, industrial CT metrology often also calls for high penetration power, as there is a need for the accurate measurement of increasingly complex metallic parts for aerospace and medical components (FIG. 5a and supplementary video 3). The region highlighted in FIG 5a contains a lattice structure designed to allow bone in-growth and better long-term attachment to surrounding bone¹¹⁵. When dimensional or geometrical measurement results have to be obtained from CT data, for example to make decisions on the conformance of the inspected products or on the control and optimization of the manufacturing processes, mere visualization of geometries and extraction of quantity values is not sufficient if the measurement uncertainty is unknown. Measurement accuracy and metrological traceability are fundamental requirements in dimensional metrology¹¹⁶.

Box 2: Time-resolved imaging

The range of length and time scales that can be imaged non-destructively by X-ray CT makes it a unique tool for acquiring 3D movies (sometimes called 4D imaging). The higher the desired resolution, the longer it takes to acquire the hundreds, or thousands, of radiographs needed for each scan. For X-ray tube sources, scans range from minutes to many hours, making them ideal for phenomena that occur over long timescales that can be followed *in situ* (for example the rising of dough or corrosion of steels), or processes that need to be monitored periodically in a time-lapse manner such as cancerous tumours, fatigue cracks in engineering structures and the changes that occur during the cycling of batteries (FIG. 5).

For rapidly changing phenomena, the simplest approach is to take advantage of the higher flux available at synchrotron sources. These enable continuous streaming where projections are collected at extremely high rates as the sample continuously rotates. Acquisition times range from several CT scans per second to study fracture²⁶⁵ to hundreds of scans per seconds to study aluminium foaming⁹⁶. For cyclic processes, this can be extended further by stroboscopic imaging, for example to analyse the biomechanics of the flight of a fly²⁶⁶. Alternatively, new CT scanning strategies are being developed around lower-cost X-ray tube sources, for example where source and detector rotate around the sample (as in Fig 1a) allowing scan times around 10 s^{8,267}, or using multiple sources to illuminate the sample from many orientations¹⁰⁴. In this way it is possible to image thousands of manufactured parts per hour using a conveyor belt.

Novel reconstruction methods can further shorten scan times and give good reconstructions using relatively few projections. This is illustrated by the imaging of a dendrite growing in molten aluminium where the number of projections was under sampled by a factor of 16 (FIG. 6 and Supplementary video 6)¹³⁰. The changes taking place during time-lapse image sequences can be quantified by correlating images to infer displacement (and hence strain) fields using **digital volume correlation [G]**^{268,269 270} or by tracking the movement of features in the imaged volume²⁷¹. One other aspect to consider for beam sensitive materials and tissues is the cumulative dose which can be significant when many scans are undertaken over a time sequence.

Good-practice procedures have been introduced for metrological CT to address different aspects. These include geometrical calibration of the scanning arrangement, the use of calibrated objects for error determination, procedures for optimising settings, metrological performance verification, etc. Interlaboratory comparisons suggest that, under specified conditions, measurement errors as small as 1/10th of a voxel are possible for simple dimensional measurements¹¹⁷. The reader is directed elsewhere for reviews on qualification and testing procedures for metrological CT systems¹¹⁸ and for examples of industrial metrology applications^{102,103,119}.

Specific software tools have been devised for metrological analyses, such as nominal-to-actual comparisons — comparisons of the measured geometry to the computer-aided design (CAD) model — and verification of dimensional and geometrical tolerances. Several algorithms have been developed to enhance the accuracy of CT measurements at different points of the CT data processing pipeline, ranging from correction of imaging artifacts to advanced methods for threshold determination and surface generation^{81,120}.

[H2] Materials Science

Materials scientists have been using microCT since the early 1990s⁷⁷ to provide a detailed picture of the internal structures of materials and their evolution during processing and/or in service. Previously, they had largely relied solely on the analysis of 2D sections (by SEM or optical microscopy) combined with stereology¹²¹. However many aspects are not easily discerned from 2D sections, such as the degree of **percolation** [G] of a phase in a sample¹²², fluid transport through a porous network¹²³ or the 3D architecture of cellular materials¹²⁴. After appropriate segmentation (as in FIG. 4), CT allows the microstructure of materials to be quantitatively analysed in terms of the number of phases, volume fraction of phases, shape, specific surface, tortuosity, etc. This precise quantitative knowledge of the microstructure is a key element for the materials scientist in understanding the relationship between processing, microstructure and structural and/or functional performance. For example, CT is uniquely able to locate defects inside a commercial battery (FIG. 5b), or to map the nature and extent of delamination impact damage layer-by-layer in a composite panel (FIG. 5d and Supplementary Video 4). It can also be used to locate features for subsequent in-depth study by higher resolution destructive electron microscopy methods¹²⁵. In materials having very fine microstructural features such as a change in morphology of battery electrode particles upon lithiation (FIG. 5c), tube or synchrotron source nano-CT²⁷ can be applied on sub-mm sized samples.

Materials scientists often exploit the high flux of synchrotron sources for real-time experiments and X-ray tube systems for longer time scale (usually time-lapse) studies. Here, the ability to track the evolution of a region of interest over the lifetime of a single sample (for example the growth of a fatigue crack in FIG. 5e where high resolution and phase contrast aid crack detection) can provide unambiguous insights into the evolutionary sequence. This contrasts with destructive longitudinal studies that rely on the statistical analysis of such features sampled at different times through the process. Indeed, for particularly rare or unpredictable events, in situ experiments significantly decrease the number of samples that need to be studied. Being able to quantify features continuously without stopping/holding/freezing the experiment also avoids questions about the validity of the features observed after holding/freezing treatments, for example in the semi-solid coarsening of metallic microstructures¹²⁶.

Time resolved imaging (BOX 2) often requires the accommodation of in situ rigs on the CT scanner sample stage to follow manufacturing processes or in-service behaviour. Some in situ studies require extremely simple sample environments. One example is the setting of plaster; once the transformation is initiated by mixing water and plaster powder, setting can be observed by repeated imaging under ambient conditions¹²⁷. Other studies, such as the solidification of metals (FIG. 6 and supplementary video 6), foaming, superplastic deformation¹²⁸, and additive manufacturing¹²⁹ require complex environments to replicate their processing conditions where the temperature (heating or cooling), the atmosphere (nature of gas and pressure) and/or the stress state (tension, compression fatigue) can be controlled.

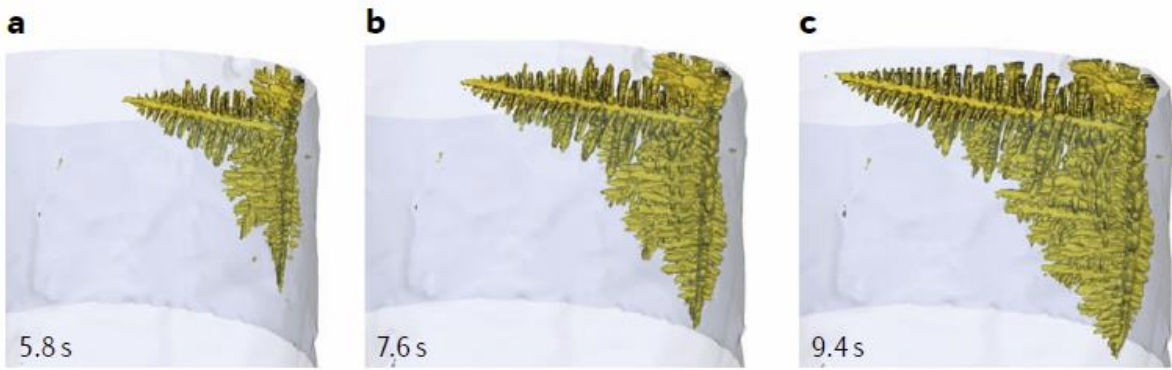


Figure 6. Real-time imaging of the solidification of an aluminium-24wt% copper alloy melt showing dendritic growth. (a) 5.8, (b) 7.6 and (c) 9.4 seconds after the start of solidification (synchrotron microCT reconstructed using iterative reconstruction)¹³⁰.

Once manufactured, a material's microstructure may evolve significantly in service according to the operating conditions. The behaviour of materials under a very wide range of in-service conditions has been studied by CT. One of the advantages of CT imaging is the ability to study how damage propagates, such as in FIG. 5e, leading up to ultimate failure for a variety of materials, strain rates¹³¹ and stress states such as tension¹³², fatigue¹³³, compression¹³⁴, indentation¹³⁵ and hydrostatic pressure¹³⁶.

Environmental conditions can also have a very strong effect on the degradation of materials in service, for example via corrosion and stress corrosion cracking¹³⁷ or exposure to high¹³⁸ or low¹³⁹ temperatures. Functional operation can also lead to structural changes; one example is the increasing use of X-ray CT, and in particular nano-CT, to study the behaviour of batteries during charging and discharging (FIG. 5b and 5c)¹⁴⁰, while high speed imaging has been used to better understand the events leading to catastrophic thermal runaway¹⁴¹.

Finally, the 3D tomographic images can also be used to produce image-based 3D simulations faithful to the microstructure by means of finite element¹⁴², discrete element¹⁴³ or Fast Fourier Transform-based¹⁴⁴ modelling. It is also possible to validate the predictive capability of such image-based models through direct comparison with the actual behaviour captured by time resolved X-ray CT imaging¹⁴⁵.

[H2] Biomedical and Life Sciences

The term biomedical imaging refers to the ex vivo, in situ, or in vivo examination of biological samples or entire animals, rather than the diagnostic scanning of patients in a hospital setting. While optical microscopy is often the imaging method of choice, X-ray CT has emerged as a powerful and versatile tool that can either complement or replace other modalities, owing to the ability of X-rays to penetrate deep into matter and the resulting opportunities for the rapid visualisation of 3D structures. X-ray CT can indeed be used for digital **histology** [G], rendering relatively large specimen sections at once and facilitating a more time-efficient analysis than traditional histopathological slicing and slice-by-slice examination under the microscope.

When the imaging task is to visualise biological tissue that is calcified (such as bone) or contains calcifications (as in FIG 2c), attenuation contrast CT is generally the appropriate method. The high X-ray attenuation of calcium provides high contrast. Indeed the quantitative imaging of bone

structure, porosity and mineral density marks the start of the application of X-ray CT in the biomedical area ¹⁴⁶ and can be used to study links between bone morphology and biological factors such as aging or drug use ¹⁴⁷. For non-calcified biomedical samples that generally exhibit weak intrinsic X-ray attenuation, contrast agents such as heavy element liquids ^{148,149} (for example iodine), gases (for example xenon ¹⁵⁰) or nano-particles can be used to locally increase the attenuation properties —and therefore the contrast — of a tissue (FIG. 1d). X-ray microCT using a tube source plays a central role in the preclinical imaging of rodents, providing an excellent visualisation of the skeletal structure ¹⁵¹ and rendering soft tissues when aided by contrast agents ¹⁵². Owing to the high soft tissue contrast achievable through iodine-staining, X-ray microCT can also be used in a clinical context, for example as a tool for scan-based post-mortem assessment of structural abnormalities in deceased foetuses ^{153,154}.

Phase contrast imaging is commonly applied when imaging soft tissue in cases where the use of contrast agents is not possible or undesirable. Phase contrast microCT can render weakly attenuating tissues with higher contrast than attenuation CT (see FIG. 2) and/or at lower dose. Phase contrast CT has been used to visualise mouse brain, revealing the molecular, granular, white matter and Purkinje cell layers of the cerebellar vermis as well as axon bundles within the white matter ¹⁵⁵. Another example where phase contrast microCT shows great promise is the intra-operative scanning of tumour-bearing breast specimens excised during cancer surgery to visualise tumour margins in 3D tissue volumes ¹⁵⁶.

The resolving power of X-ray CT readily covers the cellular length scales and beyond. For example, synchrotron microCT can render whole zebrafish with cellular resolution, allowing the identification of morphological changes linked with intrinsic (for example genetics) and extrinsic (for example environmental) factors ¹⁵⁷. NanoCT exploiting Zernike phase contrast can render cells on a polymer scaffold [G] (FIG. 5f) and can be used to quantify scaffold porosity, pore size and fibre diameter, cell length and cell diameter ¹⁰⁰, all of which can aid our understanding of cell-scaffold interaction.

X-ray CT is also opening up new opportunities across the plant ¹⁵⁸ and zoological sciences ¹⁵⁹, enabling the digital curation of data associated with new species and providing new opportunities for data sharing ^{160,161}. In ecological studies, the use of CT can assist in quantifying biological morphologies as they vary according to environmental and ecological factors ¹⁶². CT is also finding increasing use in biomimicry — where the real 3D morphology of biological structures on a microscale can be assessed for their translation to engineering solutions ¹⁶³.

[H2] Food Science

The sensory appreciation and acceptance of food products by consumers is highly correlated to their texture and microstructure. As a result, the potential of X-ray microCT in food science applications, whether fresh produce or processed food products ¹⁶⁴, is vast. X-ray microCT is particularly well-suited to the exploration of food products with foam structures, such as bread ¹⁶⁵. The microstructure of bread is determined by the spatial organisation of properties such as pore size, pore distribution and cell wall thickness. This can be visualised by scanning 20 mm-thick slices, cut from a loaf of bread, followed by digital isolation of equal sized bread crumb volumes-of-interest from the reconstructed 3D volumes ¹⁶⁵. The digitally isolated volumes-of-interest enables visualisation of the porous structure and quantification of the cell wall thickness, crumb porosity and pore size distribution. This contributes to better understanding of pore networks and in this case the effect of changes in bread formulations

on the texture and quality of the loaf. X-ray tube microCT, which requires up to an hour or even longer for image acquisition, is suitable for such applications.

Synchrotron CT scanners enable real-time imaging, for example to follow microstructural changes of ice cream¹ during thermal cycling between -15 to -5 °C. Such imaging requires an experimental setup that can maintain the sample in a frozen state (here -15 and -5 °C, respectively). In this study 3601 projections were each acquired with 0.1 s exposure time and a final pixel size of 0.8 μm before subsequent reconstruction of the 3D volume. The formation of coarse, faceted ice crystals and larger air cells due to thermal cycling is shown in FIG. 5g.

Freezing is also used in the processing of fresh produce and inevitably affects the tissue structure. Since the first non-destructive application of X-ray microCT to fresh produce in the early 1990s for the detection of maturity in green tomatoes, investigations on fruit and vegetables have characterised a range of quality factors such as produce maturity, produce decay, internal disorders of fresh fruit^{166,167} such as apples¹⁶⁸, and loss of texture in vegetables¹⁶⁹. In addition, 3D ice crystal growth has been quantified using X-ray microCT in frozen carrots stored over a period of 2 months¹⁷⁰.

[H2] Paleontology

As the only direct evidence of life that lived from a few thousand to 3.5 billion years ago, fossils are of critical significance in evolutionary biology. Their accurate interpretation is directly related to the amount of character information that can be extracted. X-ray microCT has revolutionized palaeontology by providing detailed, 3D views of structures that previously were inaccessible, or visible only through tedious and often destructive physical preparation.

X-ray imaging finds application across many length scales from large fossils embedded in tons of rock using very high energy X-rays (up to 9MeV)¹⁷¹ to micron-sized fossils in amber viewed at moderate energies (<40keV)¹⁷². Synchrotron CT, while presenting logistical stewardship issues associated with using national facilities, is providing images of extraordinary detail¹⁷³ often exploiting phase contrast. Care should also be exercised because the intense synchrotron X-ray beam can damage fossils¹⁷⁴. Amber browning¹⁷³ is perhaps the most striking example in paleontology of specimen degradation. This consideration has not prevented it be used widely, the main limitations being access to synchrotron beamlines capable of phase-contrast imaging and the small illumination area typical of these beamlines. CT scans can be converted to 3D models for myriad purposes from biomechanical analysis¹⁷⁵, to public exhibits and teaching, and for the worldwide archiving of digital facsimiles. Because the modes of fossilization vary widely, the microCT techniques employed also vary.

In permineralized fossils the organic remains, such as vertebrate bones, are replaced by minerals. If the fossil matrix differs appreciably in composition and density, microCT imaging is straightforward using standard attenuation contrast instruments. Fine internal features of bones such as lacunae, pits, and growth rings are readily discerned. The insects, plants, and vertebrates in Brazil's Early Cretaceous Crato Formation, ca. 115 million years old^{176,177} for example are exceptionally well preserved. Crato fossils such, as that in FIG. 5h, are not only preserved in 3D, but are composed of iron hydroxide, affording superior contrast against the soft limestone matrix. Imaging at relatively high energy (180 kV) provides detail of fish scales, body bristles, fine cuticle punctuation and wing veins of insects. Internal organs are preserved, but since they too are replaced by iron hydroxide,

careful (often semi-automated) segmentation is required. Small fossils replicated in silica and phosphate also exhibit extraordinary 3D preservation even of internal organs ^{178,179}.

In most deposits however, fossils are lithified — preserved as impressions or compressions of leaves, stems and insect wings in a shale or mudstone matrix. These compressions are films of carbon that are too thin and too transparent to X-rays, even with phase contrast CT.

One might expect the CT scanning of inclusions in fossil resins such as amber to be straightforward, since amber is renowned for preservation with microscopic fidelity ^{180,181}. In practice, results vary widely depending on the botanical source of the amber ¹⁸². Resins are organically complex ^{183,184}, and this affects their crosslinking, hardness, and preservative qualities. Age of amber is not a factor in the quality of the X-ray signal. Inclusions in ambers derived from *Hymenaea*, like 17–20 million year old material from the Dominican Republic and Mexico, scan very well using absorption contrast, as do insects and other life forms in 90 million year old amber from New Jersey, USA, which is derived from an extinct relative of cedars of the family Cupressaceae. In contrast, 100 million year old amber from the world's most diverse Cretaceous fossil deposit in northern Myanmar scans poorly using absorption contrast ¹⁸⁵ and better results are obtained using phase contrast at moderate kV and long scan times (for example 80kV for >20 hours ¹⁸⁶). There is little molecular integrity of chitin in the exoskeleton of insects in amber ¹⁸⁷, so organismal inclusions are typically imaged as void spaces in the amber. Interestingly, the bones of small vertebrates in amber retain excellent X-ray contrast ^{185,188,189} while soft internal organs like flight muscles in insects are commonly preserved as largely carbonized replicas but with subcellular fidelity ¹⁸⁰; these can be easily segmented since they lie in a void space of the body cavity.

[H2] Earth sciences

The unique capability of X-ray CT to provide detailed 3D and time-resolved 3D data across length scales has opened many opportunities in the earth sciences. Soil scientists and sedimentologists use X-ray CT to characterize soil and sediment, their 3D structures and the related pore network ¹⁹⁰. The optically opaque and delicate nature of soil and sediment mean that CT is well suited for exploring how biogeochemical and structural heterogeneities at the pore-scale determine their function and behaviour. X-ray CT and subsequent segmentation and analysis can provide key parameters characterising soil aggregates including particle sizes and shapes, contact points, free volume, and pore throats as a function of time or local conditions. This information helps elucidate their effect on aggregate stability ¹⁹¹, crack dynamics under repeating wetting-drying cycles ¹⁹² or the preferential transport of nutrients and contaminants along macropores. The non-destructive nature of X-ray CT is also invaluable in characterising the various components and structures (textures) of extra-terrestrial rocks ¹⁹³.

Petrography **[G]** focuses on the detailed description and identification of rocks, where the mineral content and the textural relationships within a rock are described in detail, and it is essential in classifying rock types. Currently, 3D-petrography remains challenging due to the small specimen (often a rock core) size that can be scanned at high resolution given that rock textures can extend over a wide range of length scales. To combat this, 3D data retrieved from different sample sizes, and therefore acquired at different resolutions, are often combined to generate multi-scale 3D data ¹⁹⁴. In addition to structural information, 3D chemical characterization is also crucial in the earth sciences. As standard X-ray absorption CT is not able to provide detailed chemical information, this

missing data can be partially obtained by correlative microscopy using complementary techniques such as 2D energy dispersive X-ray mapping in the SEM, X-ray Fluorescence or others. This chemical information can then be coupled to the internal structural features of the 3D scanned rocks¹⁹⁵⁻²⁰⁰ and merged into one digital model, providing multifaceted information at all the scales of interest. This information can then be used as input for image-based multi-scale pore network models to predict dynamic processes inside rocks, such as fluid flow and reactive transport²⁰¹.

Many geological applications such as hydrology, petroleum engineering, CO₂-sequestration, geothermal energy storage and water and soil remediation require a fundamental understanding of the effect of pore structure on fluid flow and mass transport. Time resolved X-ray imaging can provide unique information regarding pore scale transport processes (such as reactive transport, solute transport, and precipitation) in real-time at high spatial resolution using synchrotron micro-CT²⁰²⁻²⁰⁴ as well as a laboratory X-ray CT (FIG. 5i and Supplementary video 5)^{101,205}. The real-time monitoring of rock and soil behaviour under different stimuli can be done by either continuous or time-lapse X-ray scanning using bespoke in situ devices^{206,207}. This offers new opportunities in the earth sciences as the generated data can be used to understand transport processes and as input for 3D image-based models.

As a complement to the general purpose image segmentation and analysis software packages, custom-built in-house 3D analysis software code²⁰⁸⁻²¹⁰ specifically aimed at segmenting earth science datasets have been developed, with machine learning segmentation algorithms starting to emerge²¹¹.

[H1] Reproducibility and data deposition

Reproducibility is an important property for CT dimensional measurements. It corresponds to the closeness of agreement between the results obtained by replicate measurements on the same or similar objects, under specified conditions across different locations, operators and measuring systems¹¹⁶. In addition to reproducibility, repeatability — repeated multiple measurements on the same system — is an inherent requirement for all measurement methods. Well-defined scanning and analysis protocols ensure reproducibility and repeatability. Accuracy of measurements depends on the CT system as well as on all the other possible error sources. To achieve good accuracy, both random and systematic errors need to be small¹¹⁶. The uncertainty of CT measurements depends on many factors, which may be grouped as shown in Table 1.

In addition to general improvements in the performance of CT systems, such as higher spatial resolution and augmented computing capability, metrological CT systems have undergone several advancements that have enhanced their precision and helped achieve metrological traceability. For example, metrology CT systems now include temperature-controlled cabinets and other means to reduce or compensate for errors induced by thermal effects during X-ray acquisition. Other specific hardware improvements to the X-ray machines include accurate displacement encoders and high-precision manipulators, with positioning errors depending also on the mass of the sample being measured. Some metrological CT systems are equipped with additional measuring sensors, for example mechanical or optical probing units, which are used to correct the errors in CT measurements and enable multisensor data fusion²¹². Such advanced correction tools are particularly useful for applications demanding higher accuracy, since conventional CT systems are subject to several potential errors and artifacts.

Further details on the influencing variables and their effects on CT measurement results can be found in the VDI/VDE 2630 guidelines^{213, 214} which also discuss the main image artifacts. ASTM standards also provide guidelines for performance verification of CT systems^{215,216}, while the International Organization for Standardization (ISO) is currently developing new standards for metrological performance verification are under development¹¹⁸.

Metrological traceability is fundamental for the reliability of a measurement result, since accuracy cannot be assured without establishing traceability to the measurement unit. Traceability ensures that the measured quantity is related to the international definition of the unit with which it is expressed (i.e. the metre for dimensional measurements) through an unbroken chain of calibrations¹¹⁶. To achieve traceability, not only are qualification and testing of CT systems¹¹⁸ important requirements, but calibration and uncertainty determination are also needed. Different methods are currently used or under development for calibration^{217,218} and uncertainty determination^{219,220}. In particular, the measurement uncertainty is task-specific since it depends on the actual measurement conditions, as documented in recent interlaboratory comparisons using calibrated reference objects^{117,221,222}.

Spatial resolution is one of the factors determining measurement uncertainty, although just one of many (as is clear from the numerous influencing variables listed in Table 1). Spatial resolution depends on several factors beyond the voxel size including, for example, the focal spot size and drift (see¹¹⁸ for more details). In addition to the factors that affect the spatial resolution in the tomogram, other factors influence the resolution of the obtained measurement data (also referred to as the metrological structural resolution²²³); such additional factors include software operations that are performed in several phases of data processing and surface determination^{224,225}. Recent research has also documented the variability introduced by different thresholding methods applied in segmentation and surface determination^{120,226}.

Table 1: Influencing variables affecting the uncertainty of CT measurements

Category	Examples of influencing variables
CT system	X-ray source, detector, axes, hardware filtering, other components of the CT machine.
Application	Object material(s) and geometry, fixturing, scanning parameters, reconstruction parameters, other settings.
Analysis	Algorithms and software for reconstruction, segmentation and data analysis.
Environment	Temperature, humidity, vibrations, other ambient conditions.
Operator	Operator's choices on the measurement procedure and its implementation.

Image datasets can be large: currently \sim 50 Gb per volume for single scans, and a few Tb for 4D studies. This presents issues for the transportation and archiving of such datasets. Nevertheless

there are a number of image repositories emerging that are able to archive 3D image data across various fields (for example; digitalrocksportal.org, digimorph.org, digitalfishlibrary.org, paleo.esrf.eu, morphosource.org, morphomuseum.com, phenome10k.org, Gigabytejournal.com, data.mendeley.com, materialsdatafacility.org) [Au: [hyperlinks](#)]. While there are no current standards for sharing CT data, the minimum requirement is to provide the voxel size of the dataset and its format (usually assumed to be.tiff image stacks). Additional information relating to the scanner system used, voltage and current settings and number of projection images used and reconstruction algorithm should also be provided.

[H1] Limitations and optimizations

[H2] Dose effects

While X-ray CT is widely accepted to be non-destructive, as discussed in the introduction, the dose required to obtain a satisfactory tomogram increases as the reciprocal of the fourth power of the voxel size. This, and the fact that synchrotron sources are of extremely high flux, mean that both high doses and high flux can lead to radiation damage and artifacts, even for materials largely considered insensitive to damage. These can include localised heating-induced effects as well as structural damage, such as discolouration, chemical changes, and, in the case of biological samples, damage to DNA. Beam damage happens when X-rays and matter interact by means of photoelectric absorption (which dominates at energies <30 keV), generating secondary photons or photoelectrons, and/or sample heating. As a result, high energy X-rays are less damaging than low energy ones. With regards to sample heating, the high X-ray flux available at synchrotron sources mean this can be significant especially for white beam nanoCT²²⁷, but is typically not an issue for tube source CT.

Structural damage to polymers and biological samples can be minimised by cooling samples to liquid helium temperature where structural damage becomes significant only at doses $>10^8$ Gy (Gray [G]), enabling CT at tens of nanometer resolution²²⁸. DNA damage in vivo has been illustrated in animal models at room temperature at much lower doses ($\sim 1-20$ Gy)²²⁹, implying that DNA damage occurs for CT at much lower resolutions. For tube source microCT operating at 100kV, the dose for 10 μ m CT has been reported to be around 0.4 Gy^{230,231}, while for medical CT scanning a head scan might require a dose of around 0.06 Gy³. Because the effect of the radiation dose on the body changes with the radiation type and energy the [effective dose \[G\]](#), measured in milliSieverts (mSV), is often used to assess the risk to human health. Levels above 200mSv have been shown to give rise to a small but significant increase in cancer risk³. In the case of sub-fossil bones 200Gy has been identified as the safe limit¹⁷⁴, leading to the conclusions that CT voxel sizes should therefore be greater than 1 μ m to limit the damage to fossil DNA and that the addition of a metallic filter in front of the source can have significant benefits for tube source CT, because it removes the lowest energy, and thus the most damaging, X-rays.

Phase contrast CT can lead to dose benefits over attenuation CT^{232,233}. The δ term (Eqn 1), that delivers phase contrast, decreases less rapidly with increasing energy compared to the attenuation term β , permitting the use of a higher energy and less damaging beam while not suffering as much loss in contrast. Indeed, under certain experimental conditions (for example high resolution scanning or scanning a sample composed of similar materials) phase contrast CT can also yield a better signal-to-noise ratio than attenuation CT at the same dose or lower^{234,235}.

[H2] Imaging artifacts

Unless recognised, and where possible accounted for, imaging artifacts can seriously affect the interpretation of X-ray tomograms. In this Primer, we mention a few of the most common types of artifacts and point the reader towards strategies for their minimisation or correction.

Concentric ring artifacts (FIG. 7a) of alternating contrast can arise in reconstructions due to the differential response of individual detector pixels, even after flat field correction. These can be eliminated during acquisition by translating the detector between projections²³⁶ or, more commonly, corrected for during reconstruction. Beam hardening artifacts (FIG. 7b), evident as uneven contrast (cupping) between the middle and edges of high atomic number materials, arise when imaging with polychromatic X-ray radiation, because the softer X-ray radiation is preferentially removed in paths intersecting the sample centre compared to paths through the periphery. To reduce beam hardening, beam filtering is often used with an absorptive material (for example a copper plate typically of 0.5 mm thickness) to pre-emptively absorb the low-energy X-rays and harden the beam before it reaches the sample. Limited projection artifacts (FIG.7c) are windmill shaped artifacts (or bear claw artifacts in the case of helical scan patterns) that arise when too few projections are used to reconstruct the image. It is clear by comparing the reconstructed slices in FIG. 7c and 7e (right) that, for 30 projections, there are characteristic artifacts and the internal porosity cannot be discerned. Iterative reconstruction algorithms offer the potential for high quality reconstruction when the data is very noisy and sparse; machine learning also can ameliorate the effects of undersampling⁷⁴.

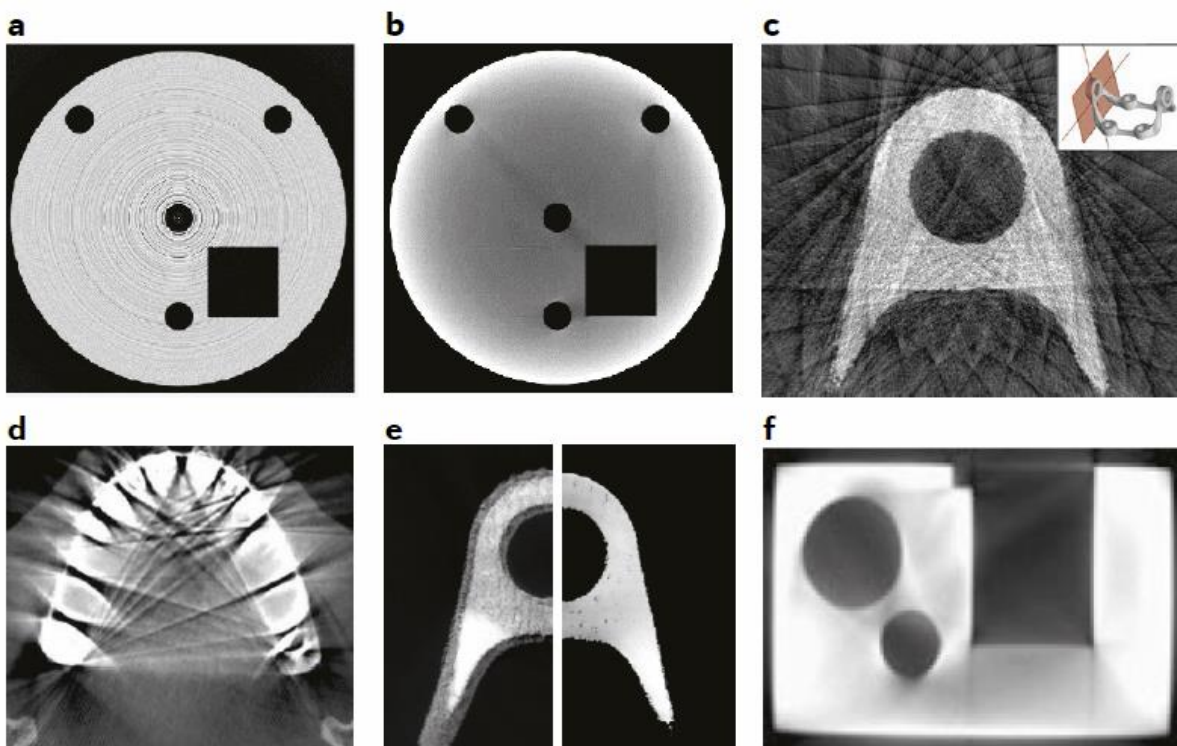


Figure 7: Virtual CT slices illustrating common reconstruction artifacts. a) ring artifacts²³⁷; b) beam hardening artifacts²³⁷; c) limited (here, 30) projection reconstruction of a titanium additively manufactured bracket (see inset for the full component); d) streak artifacts in a section of upper jaw due to silver amalgam crowns²³⁸; e) titanium additively manufactured bracket with (left) and without (right) motion artifact; f) cone beam distortion²³⁹.

Phase contrast artifacts are evident as light/dark fringes that can be seen at phase boundaries when the beam has some degree of coherence. These can aid boundary location but they distort the image contrast locally. The partial volume effect occurs when partially-filled voxels towards the edge of objects take an intermediate greyscale. This can lead to problems when greyscale thresholding, especially if the feature of interest is only represented by a few voxels. Streaking artifacts (FIG. 7d) can have a number of causes, but the most common relates to almost complete attenuation (i.e. photon starvation) by high density objects, or the limited dynamic range of the detector. Motion artifacts (FIG. 7e) arise from movement during the acquisition process and can be intrinsic (such as a heartbeat) or extrinsic (such as beam damage or the drying of a hydrated specimen). Artifacts can also arise if the centre of rotation is off-centre or the sample wobbles with respect to it. The latter can be corrected by realigning the projections in the sinogram during reconstruction. As mentioned earlier, iterative reconstruction methods can give high-quality reconstructions even when the data is highly under-sampled allowing lower dose/faster timeframe scanning²²⁴ thereby minimising movement during a scan (see Fig 6). Cone beam artifacts are specific to cone beam setups (FIG 1b) and can introduce geometrical distortions — as shown in the straight sides of the image in FIG. 7f — and become increasingly serious with distance from the central slice. They arise because the filtered back projection reconstruction method is strictly valid only for the central slice.

[H2] Field of view/spatial resolution issues

Modern detectors often have between 1000×1000 to 4000×4000 pixels. This creates a trade-off, as with all imaging methods, between the resolution and field of view, although this can be somewhat mitigated by stitching together multiple images leading to much larger tomograms²⁴⁰. Given that features of interest should often be at least three times, and ideally ten times, larger than the voxel size to positively be identified this makes detecting small features such as cracks or critical defects (such as those introduced during additive manufacturing) a challenge in realistically-sized components.

One way to mitigate this is to perform local (region of interest) tomography. Contrary to popular understanding²⁴¹, having material outside the field of view need not introduce serious imaging artifacts; while there can be shifts in the contrast values, the geometry within the region of interest is not generally affected^{242,243}. In many cases the diameter of the object can be as much as ten times larger than the field of view without significant artifacts other than a slight cupping²⁴⁴. However, scanning a small section of a large part may not always be practical (depending on sample geometry), or for attenuating materials it may require excessive scan times or very hard X-rays.

A major challenge is also posed by the size of data generated for high temporal and spatial resolution data. Time-resolved datasets can be many hundreds of gigabytes and present significant challenges in storing, analysing, and visualising the data. Consequently, analysing 3D and 4D data requires large computing power along with expertise in specialized software packages.

[H1] Outlook

The last thirty years has seen a dramatic increase in spatial resolution, a shortening of the time and a lowering of the dose needed to acquire CT scans through a combination of improved sources (both synchrotron and laboratory tube sources), detectors and reconstruction algorithms. There is little reason to believe that this progress will stall. Compact light sources⁵⁴, liquid metal sources⁵³,

microstructured targets²⁴⁵ and laser driven sources²⁴⁶ are increasing the attainable fluxes and phase contrast and bridging the gap between tube and synchrotron sources, while nanoCT enables the investigation of microstructures too fine to be discerned by microCT. In line with such developments, the diversity of applications in CT continues to grow as its capabilities are being extended and recognized in new areas, for example in the food sciences, cultural heritage², and forensics^{247,248}, where the traceability of the inspection is particularly useful for legally sensitive situations as the data can be kept on record. As CT capabilities continue to improve other areas will emerge, particularly in the life sciences.

The frame rates of both synchrotron and tube source CT has increased markedly over recent years, enabling real-time imaging across a wide range of processes. This trend is being accelerated by new iterative algorithms able to produce high quality images at lower doses and for fewer projections⁷³. The drive towards faster acquisition will benefit from the use of multiple X-ray tube sources to collect many projections in rapid succession²⁴⁹, which could see CT as an online inspection tool for manufacturing¹⁰⁴. For the monitoring of structural changes and deformation by **digital volume correlation [G]** the preliminary acquisition of a good quality scan and the subsequent calculation of the deformation field based on only a few radiographs opens up the possibility of faster mapping in the laboratory as opposed to at a synchrotron²⁵⁰.

At present, the development of automated procedures for the segmentation and analysis of 3D images requires a high level of expertise. Manual intervention is all too commonly required to segment complex low contrast microstructures. Emerging machine learning approaches^{86,211} promise to lower the level of expertise required to segment complex images (such as X-ray in histotomography¹⁵⁷), as well as to automatically identify critical defects or features.

New imaging modalities and methods continue to emerge and advance. For example, the development of dual-energy CT where two images are collected (either in sequence or simultaneously²⁵¹) at different accelerating voltages. This provides some level of elemental discrimination as well as increased sensitivity when imaging objects containing both highly and lowly attenuating phases. This approach has been taken further with the development of **spectral CT [G]**, using detectors that apportion the detected photons to a few energy channels, and **hyperspectral CT [G]**, using detectors having many energy channels. These techniques provide some level of elemental selectivity^{252,253}. They are beginning to find application in medical imaging to enhance tissue contrast, and have great potential in security and industrial scanning, as well as in earth and materials science where the ability to map elemental composition would be valuable. Diffraction-based tomographic methods²⁵⁴⁻²⁵⁸ are being developed that are sensitive to local crystallography and can image discrete phases, grain structures, lattice parameter variations, and distribution of nanocrystalline vs. amorphous phases that cannot be discriminated by conventional attenuation and phase contrast CT. Dark field methods^{259,260} and **ptychography [G]**²⁶¹ have further extended the contrast modes and resolutions that can be achieved.

Finally, tomography is being increasingly combined with other methods to build up a more complete picture within correlative frameworks^{125,262}, for example as a means of covering a wider range of length scales, to provide complementary information, or to steer and direct subsequent destructive measurements²⁶³.

Supplementary videos

Supplementary video 1: 3D rendering of the head of a 49 million year old Huntsman spider (*Eusparassus crassipes*) in dark (largely opaque) fossilised amber (phase contrast enhanced tube source microCT)²⁶⁴.

Supplementary video 2: 3D rendering of the pupation of a Painted Lady butterfly chrysalis (tube source microCT)⁷.

Supplementary video 3: Dimensional metrology of the lattice structure within an additively manufactured Ti alloy biomedical implant (tube source microCT, image courtesy du Plessis)

Supplementary video 4: 3D rendering of impact damage in a $[(0^\circ/90^\circ)_2]_s$ carbon fibre reinforced polymer (CFRP) panel subjected to impact damage (energy 20J) (recorded on tube source microCT)⁹⁹.

Supplementary video 5: time lapse 3D rendering showing the infiltration of Savonnières limestone with caesium chloride (Tube source microCT).¹⁰¹

Supplementary video 6: Real-time imaging of the solidification of an aluminium-24wt% copper alloy melt showing dendritic growth (synchrotron microCT reconstructed using iterative reconstruction)¹³⁰.

Acknowledgements

PJW would like to acknowledge funding from the European Research Council under grant ERC under grant CORREL-CT No. 695638.

Author contributions

Introduction (P.J.W); Experimentation (S.R.S., C.K.H); Results (C.B., S.R.S., P.J.W)); Applications (E.M., S.C., C.K.H., V.C., D.G., P.J.W); Reproducibility and data deposition (A.P., S.C.); Limitations and optimizations (P.J.W., C.B., S.C., A.P., S.R.S.); Outlook (P.J.W., C.B., S.C., V.C., D.G., C.K.H., E.M., M.M., A.P., S.R.S.); Overview of the Primer (P.J.W.).

Key Reading

Stock, S. R. MicroComputed Tomography: Methodology and Applications. 2nd edn, (Taylor and Francis, 2019).

This monograph is designed for those new to microtomography and covers the fundamentals in an integrated fashion and includes many examples of applications, grouped not by subject discipline but by

Kak, A. C. & Slaney, M. Principles of Computerized Tomographic Imaging. (SIAM (Soc. Industrial Appl. Math.), 2001).

This book provides a tutorial style introduction to the algorithms used for reconstructing CT images from projection data.

Bultreys, T. *et al.* Fast laboratory-based micro-computed tomography for pore-scale research: Illustrative experiments and perspectives on the future. *Advances in Water Resources* **95**, 341-351, doi:<https://doi.org/10.1016/j.advwatres.2015.05.012> (2016).

While challenges do persist in the field of earth sciences to image a rock's pore space in 3D, this article considers the next frontier in laboratory-based micro-CT scanning: in-situ, time-resolved imaging of dynamic processes.

Maire, E. & Withers, P. J. Quantitative X-ray Tomography. *International Materials Reviews* **59**, 1-43, doi:<http://dx.doi.org/10.1179/1743280413Y.0000000023> (2014).

This invited paper reviews the field of tomography with special emphasis on the capability of the technique quantification and analysis.

S. Carmignato, W. Dewulf, R. Leach, Industrial X-ray Computed Tomography, Springer, 2018;
<https://doi.org/10.1007/978-3-319-59573-3>

Comprehensive book covering all aspects of industrial and scientific X-ray computed tomography, including basics, metrology, calibration and applications.

Rawson, S. D., Maksimcuka, J., Withers, P. J. & Cartmell, S. H. X-ray computed tomography in life sciences. *BMC Biology* **18**, 21, doi:10.1186/s12915-020-0753-2 (2020).

Introduction to the possibilities offered by X-ray CT in the life sciences.

Paganin, D., Mayo, S. C., Gureyev, T. E., Miller, P. R. & Wilkins, S. W. Simultaneous phase and amplitude extraction from a single defocused image of a homogeneous object. *J. Microscopy* **206**, 33-40 (2002).

This paper describes the most widely used phase retrieval method in propagation-based phase contrast CT, implying that 3D volumes of phase can be reconstructed from a single radiograph per angle, thus allowing for rapid and practicable imaging.

Glossary (in order of appearance)

radiographs: a radiograph is an image formed by X-rays transmitted through an object, originally collected on a photographic plate but now acquired digitally.

projections: a projection is a radiograph of the object acquired at a given angle of illumination which, when combined with many others, provides the data for numerically reconstructing the object. Normally between 100 and 3600 projections are used to reconstruct a tomogram.

greyscale: a synonym for the range of voxel values within a slice or volume or tomographic data set

tomogram: originally a 2D slice through the object reconstructed computationally from a sinogram. Now often used to refer to the 3D reconstructed image.

attenuation contrast: contrast in a radiograph or tomogram resulting from differences between the intrinsic attenuation of components in an object

phase contrast: contrast in a radiograph or tomogram resulting from the difference in phase developed by beams as they pass through an object

linear attenuation coefficient (μ): a measure of how easily X-rays can penetrate a material. It is given by the fraction of incident photons in a monoenergetic beam that are attenuated per unit thickness of that material.

temporal resolution: this is defined by the time required to acquire enough projections, of sufficient signal to noise ratio, to reconstruct an image of the desired quality. The time per scan can often be shortened by using fewer projections combined with iterative reconstruction techniques.

pixels: abbreviation for picture element, a pixel is the basic digital unit of a two-dimensional image or radiograph

voxels: an abbreviation for a volume element (by analogy with picture element and pixel), a voxel is the basic unit of a three-dimensional digital representation of an image or object. The voxel size should not be confused with the spatial resolution.

spatial resolution: smallest linear distance between two points that can be distinguished in the reconstructed image. Usually considerably larger than the voxel size, depending on the scanned materials and the scanning conditions.

contrast agents: highly attenuating particles, gases or stains used to increase the X-ray attenuation contrast of specific structures or defects.

monochromatic beam: a beam (of X-rays) containing photons with a single energy (wavelength) or a narrow range of energies

polychromatic (white): beam: a beam (of X-rays) containing photons having a wide range of wavelengths. Typical of X-ray tube sources, but also is available at some synchrotron beamlines. For tube sources, the accelerating voltage determines the maximum X-ray energy but the majority of the X-ray photons have a much lower energy.

X-ray tube: a relatively low cost and compact source of polychromatic X-rays, typically used in cone beam tomography, producing X-rays by accelerating energetic electrons into a metal target with the subsequent deceleration producing a divergent beam of broad spectrum of X-ray energies along with characteristic peaks.

Synchrotron: a large-scale facility in which electrons circulate continuously around an essentially circular path defined by bending magnets. Bending magnets and insertion devices deflect the electrons thereby creating X-ray beams tangential to the ring.

X-ray flux: number of X-ray photons in the incident beam per second per unit area

accelerating voltage: the electrical potential difference which accelerates the electrons that produce X-rays; this voltage determines the maximum X-ray energy

bending magnets: used to maintain the trajectory of the electrons in a synchrotron storage ring.

They produce x-rays over continuous spectrum and are typically much less intense and less focused than the beam of X-rays from an insertion device.

insertion devices: magnetic devices used in a synchrotron to produce X-rays from the circulating electrons

flat field correction: an image collected without the specimen in place. It is used to correct for the different sensitivity of each pixel in the detector or non-uniformities across the x-ray beam

laminography: a variant of X-ray CT suited to the imaging of flat objects

absorption edges: characteristic sharp discontinuities in the absorption spectrum of a substance that are related to the sharply defined energy levels that electrons occupy in the atoms of a given element.

coherent radiation: an X-ray beam where all the photons in a plane have the same (wave) phase

segmentation: an image processing procedure of assigning a label to every voxel in a volume such that voxels with the same label share certain characteristics

volume rendering: three-dimensional representation of data, often with certain segmented regions colourized or rendered transparent.

Radon transform: is an integral transform that projects a cross sectional slice along a given direction to give the 1D profile. In X-ray CT the plot of the Radon transform for a slice is represented by a sinogram.

sinogram: a graph created by plotting the signal recorded by a line of voxels as the sample (or source and detector) is rotated through 180°.

greyscale thresholds: greyscale levels used in an image processing procedure to segment a reconstructed volume based on the greyscale value of the voxel being above or below the given thresholds.

histogram: a graph that shows how many times an event occurs across various groups of data or classes. Often used to display the frequency of greyscale levels recorded in a tomogram.

partial volume effect: the appearance of greyscale levels in reconstructed data intermediate between those corresponding to two constituent materials when the voxel is partially filled by both. Simple greyscale threshold methods can mis-segment such voxels.

pore throats: characterises the smallest cross-sectional area of a pore channel and is equal to the radius of a circle drawn perpendicular to fluid flow at the narrowest point

tortuosity: describes how winding a path or shape is. It is defined as the ratio of actual path length to the straight distance between the ends of the path.

ortho-sections or ortho-slices: three orthogonal virtual slices through the volume.

region of interest scanning: normally CT scans include the whole of the sample width in the field of view, but in cases where higher resolution is required than this allows, it is possible to reconstruct datasets for which a smaller field of view is present in all of the projections, albeit with the introduction of some imaging artifacts such as uneven contrast.

percolation: the measure of the connectivity of a constituent domain in an object.

histology: the branch of biology studying tissues by optical or other microscopies.

scaffold: a structure that “supports” tissue and is at the core of many tissue engineering applications.

petrography: the branch of petrology dealing with the description and classification of rocks, especially by microscopic examination.

Gray: unit of radiation dose absorbed. It is equal to the absorption of one joule of radiation energy per kilogram of matter being irradiated.

effective dose: expressed in millisieverts (mSv), it is the dose calculated for the whole body taking into account not only the nature of the incoming radiation but also the sensitivities of all the organs to radiation.

digital volume correlation: a method of correlating the location of features between successive observations (here CT scans) in order to map material movement, deformation or strain in 3D.

Spectral CT: The acquisition of several CT reconstructions with the collected photons apportioned to a small number of energy channels on the basis of which some level of elements differentiation can be undertaken

hyperspectral CT: assigns the detected photons to many energy channels enabling CT reconstructions as a function of energy, on the basis of which different elements can be differentiated, often on the basis of their characteristic absorption edges.

Ptychography a computational imaging technique where the image is computationally reconstructed from many coherent interference patterns

Radon Transform The radon transform takes a projection of a 2D slice along a direction to give the 1D line profile.

References

- 1 Guo, E. Y. *et al.* Synchrotron X-ray tomographic quantification of microstructural evolution in ice cream - a multiphase soft solid. *RSC Adv.* **7**, 15561-15573, doi:10.1039/c7ra00642j (2017).
- 2 Morigi, M. P., Casali, F., Bettuzzi, M., Brancaccio, R. & D'Errico, V. Application of X-ray Computed Tomography to Cultural Heritage diagnostics. *Applied Physics A* **100**, 653-661, doi:10.1007/s00339-010-5648-6 (2010).
- 3 McCollough, C. H., Bushberg, J. T., Fletcher, J. G. & Eckel, L. J. Answers to Common Questions About the Use and Safety of CT Scans. *Mayo Clin. Proc.* **90**, 1380-1392, doi:10.1016/j.mayocp.2015.07.011 (2015).
- 4 Seeram, E. *Computed Tomography: Physical Principles, Clinical Applications, and Quality Control*. 4th ed. edn, 576 (Elsevier, 2015).
- 5 Carmignato, S., Dewulf, F. W. & Leach, R. *Industrial X-ray Computed Tomography*. (Springer, 2018).
- 6 Withers, P. J. & Preuss, M. Fatigue and Damage in Structural Materials Studied by X-Ray Tomography. *Annual Review of Materials Research* **42**, 81-103, doi:10.1146/annurev-matsci-070511-155111 (2012).
- 7 Lowe, T., Garwood, R. J., Simonsen, T. J., Bradley, R. S. & Withers, P. J. Metamorphosis revealed: time-lapse three-dimensional imaging inside a living chrysalis. *Journal of the Royal Society Interface* **10**, 20130304 doi:10.1098/rsif.2013.0304 (2013).
- 8 Van Offenwert, S., Cnudde, V. & Bultreys, T. Pore-Scale Visualization and Quantification of Transient Solute Transport Using Fast Microcomputed Tomography. *Water Resources Research* **55**, 9279-9291, doi:10.1029/2019WR025880 (2019).
- 9 Proudhon, H., Moffat, A., Sinclair, I. & Buffiere, J.-Y. Three-dimensional characterisation and modelling of small fatigue corner cracks in high strength Al-alloys. *Comptes Rendus Physique* **13**, 316-327, doi:<https://doi.org/10.1016/j.crhy.2011.12.005> (2012).
- 10 Finegan, D. P. *et al.* In-operando high-speed tomography of lithium-ion batteries during thermal runaway. *Nature Communications* **6**, doi:10.1038/ncomms7924 (2015).
- 11 Als-Nielsen, J. & McMorrow, D. *Elements of Modern X-Ray Physics*. (Wiley, 2010).
- 12 Hsieh, J. *Computed Tomography Principles, Design, Artifacts, and Recent Advances*. 3rd ed. edn, 574 (SPIE Press, 2015).
- 13 Stock, S. R. *et al.* *Tomography with energy dispersive diffraction*. in *Developments in X-ray Tomography XI* Vol. 10391 (ed Bert Mueller) 103910A (SPIE, 2017).
- 14 Schuren, J. C. *et al.* New opportunities for quantitative tracking of polycrystal responses in three dimensions. *Curr Opinion Sol State Mater Sci* **19**, 235-244 (2015).
- 15 Dierolf, M. *et al.* Ptychographic X-ray computed tomography at the nanoscale. *Nature* **467**, 436-439, doi:10.1038/nature09419 (2010).
- 16 Lionheart, W. R. B. & Withers, P. J. Diffraction tomography of strain. *Inverse Problems* **31**, 45005-45005 (2015).
- 17 Ludwig, W., Schmidt, S., Lauridsen, E. M. & Poulsen, H. F. X-ray diffraction contrast tomography: a novel technique for three-dimensional grain mapping of polycrystals. I. Direct beam case. *Journal of Applied Crystallography* **41**, 302-309, doi:10.1107/s0021889808001684 (2008).
- 18 Poulsen, H. H. *Three-Dimensional X-ray Diffraction Microscopy*. (Springer, 2004).
- 19 Birkbak, M. E., Leemreize, H., Frolich, S., Stock, S. R. & Birkedal, H. Diffraction scattering computed tomography: a window into the structures of complex nanomaterials. *Nanoscale* **7**, 18402-18410, doi:10.1039/c5nr04385a (2015).
- 20 Guizar-Sicairos, M., Georgiadis, M. & Liebi, M. Validation study of small-angle X-ray scattering tensor tomography. *Journal of Synchrotron Radiation* **27**, 779-787, doi:doi:10.1107/S1600577520003860 (2020).

21 Simionovici, A. *et al.* X-ray fluorescence microtomography: Experiment and reconstruction.in *Developments in X-ray Tomography II* Vol. SPIE Proc Vol 3772 (ed U. Bonse) 304-310. (SPIE, 1999).

22 Sullivan, L. H. The tall office building artistically considered. *Lippincott's Monthly Magazine* **57**, 403-409 (1896).

23 Stock, S. R. *MicroComputed Tomography: Methodology and Applications*, . 2nd edn, (Taylor and Francis, 2019).

24 Maire, E. & Withers, P. J. Quantitative X-ray Tomography. *International Materials Reviews* **59**, 1-43, doi:<http://dx.doi.org/10.1179/1743280413Y.0000000023> (2014).

25 Stock, S. R. X-ray Microtomography of Materials. *Int. Mat. Reviews* **44**, 141-164 (1999).

26 Wong, M. D., Spring, S. & Henkelman, R. M. Structural Stabilization of Tissue for Embryo Phenotyping Using Micro-CT with Iodine Staining. *PLOS ONE* **8**, e84321, doi:10.1371/journal.pone.0084321 (2014).

27 Withers, P. J. X-ray Nanotomography. *Materials Today* **10**, 23-34 (2007).

28 Gondrom, S. *et al.* X-ray computed laminography: an approach of computed tomography for applications with limited access. *Nuclear Engineering and Design* **190**, 141-147, doi:[http://dx.doi.org/10.1016/S0029-5493\(98\)00319-7](http://dx.doi.org/10.1016/S0029-5493(98)00319-7) (1999).

29 Grodzins, L. Optimum energies for x-ray transmission tomography of small samples - applications of synchrotron radiation to computerized-tomography .1. *Nuclear Instruments & Methods in Physics Research* **206**, 541-545, doi:10.1016/0167-5087(83)90393-9 (1983).

30 Coursey, C. A. *et al.* Dual-energy multidetector CT: how does it work, what can it tell us, and when can we use it in abdominopelvic imaging? *Radiographics* **30**, 1037-1055 (2010).

31 Hellerhoff, K. *et al.* Assessment of intraductal carcinoma in situ (DCIS) using grating-based X-ray phase-contrast CT at conventional X-ray sources: An experimental ex-vivo study. *PLOS ONE* **14**, e0210291, doi:10.1371/journal.pone.0210291 (2019).

32 Bravin, A., Coan, P. & Suortti, P. X-ray phase-contrast imaging: from pre-clinical applications towards clinics. *Physics in Medicine and Biology* **58**, R1-R35, doi:10.1088/0031-9155/58/1/r1 (2012).

33 Wilkins, S. W. *et al.* On the evolution and relative merits of hard X-ray phase-contrast imaging methods. *Philosophical Transactions of the Royal Society a-Mathematical Physical and Engineering Sciences* **372**, doi:10.1098/rsta.2013.0021 (2014).

34 Endrizzi, M. X-ray phase-contrast imaging. *Nuclear Instruments and Methods in Physics Research Section A: Accelerators, Spectrometers, Detectors and Associated Equipment* **878**, 88-98, doi:<https://doi.org/10.1016/j.nima.2017.07.036> (2018).

35 Wen, H. *Biomedical X-Ray Phase-Contrast Imaging and Tomography*.in *Springer Handbook of Microscopy* (eds P.W. Hawkes & J.C.H. Spence) (Springer Handbooks. Springer, 2019).

36 Brennan, S. & Cowan, P. L. A suite of programs for calculating x-ray absorption, reflection, and diffraction performance. *Review of Scientific Instruments* **63**, 850-853, doi:10.1063/1.1142625 (1992).

37 Henke, B. L., Gullikson, E. M. & Davis, J. C. X-ray interactions: photoabsorption, scattering, transmission and reflection at E = 50-30000 eV, Z = 1-92. *Atomic Data and Nuclear Data Tables* **54**, 181-342, doi:10.1006/adnd.1993.1013 (1993).

38 Snigirev, A., Snigireva, I., Kohn, V., Kuznetsov, S. & Schelokov, I. On the possibilities of x-ray phase contrast microimaging by coherent high-energy synchrotron radiation. *Review of Scientific Instruments* **66**, 5486-5492 (1995).

39 Wilkins, S. W., Gureyev, T. E., Gao, D., Pogany, A. & Stevenson, A. W. Phase-contrast imaging using polychromatic hard X-rays. *Nature* **384**, 335-338 (1996).

40 Cloetens, P. *et al.* Holotomography: Quantitative phase tomography with micrometer resolution using hard synchrotron radiation x rays. *Applied Physics Letters* **75**, 2912-2914, doi:10.1063/1.125225 (1999).

41 Schmahl, G. *et al.* Phase contrast studies of biological specimens with the x-ray microscope at BESSY (invited). *Review of Scientific Instruments* **66**, 1282-1286, doi:10.1063/1.1145955 (1995).

42 Hofsten, O. v., Bertilson, M., Lindblom, M., Holmberg, A. & Vogt, U. Compact Zernike phase contrast x-ray microscopy using a single-element optic. *Opt. Lett.* **33**, 932-934, doi:10.1364/OL.33.000932 (2008).

43 Sakdinawat, A. & Liu, Y. Phase contrast soft x-ray microscopy using Zernike zone plates. *Optics Express* **16**, 1559-1564, doi:10.1364/OE.16.001559 (2008).

44 Stampanoni, M. *et al.* Phase-contrast tomography at the nanoscale using hard x rays. *Physical Review B* **81**, 140105, doi:10.1103/PhysRevB.81.140105 (2010).

45 Holzner, C. *et al.* Zernike phase contrast in scanning microscopy with X-rays. *Nat Phys* **6**, 883-887, doi:<http://www.nature.com/nphys/journal/v6/n11/abs/nphys1765.html#supplementary-information> (2010).

46 David, C., Nohammer, B., Solak, H. H. & Ziegler, E. Differential x-ray phase contrast imaging using a shearing interferometer. *Applied Physics Letters* **81**, 3287-3289, doi:10.1063/1.1516611 (2002).

47 Momose, A. *et al.* Demonstration of X-Ray Talbot interferometry. *Japanese Journal of Applied Physics Part 2-Letters & Express Letters* **42**, L866-L868, doi:10.1143/jjap.l866 (2003).

48 Pfeiffer, F., Weitkamp, T., Bunk, O. & David, C. Phase retrieval and differential phase-contrast imaging with low-brilliance X-ray sources. *Nature Physics* **2**, 258-261 (2006).

49 Davis, T. J., Gao, D., Gureyev, T. E., Stevenson, A. W. & Wilkins, S. W. Phase-contrast imaging of weakly absorbing materials using hard x-rays. *Nature* **373**, 595-598, doi:10.1038/373595a0 (1995).

50 Ingal, V. N. & Beliaevskaya, E. A. X-ray plane-wave topography observation of the phase contrast from a non-crystalline object. *Journal of Physics D: Applied Physics* **28**, 2314-2317, doi:10.1088/0022-3727/28/11/012 (1995).

51 Olivo, A. & Speller, R. A coded-aperture technique allowing x-ray phase contrast imaging with conventional sources. *Applied Physics Letters* **91**, 074106, doi:10.1063/1.2772193 (2007).

52 Krenkel, M., Töpperwien, M., Dullin, C., Alves, F. & Salditt, T. Propagation-based phase-contrast tomography for high-resolution lung imaging with laboratory sources. *AIP Advances* **6**, 035007, doi:10.1063/1.4943898 (2016).

53 Larsson, D. H., Vågberg, W., Yaroshenko, A., Yildirim, A. Ö. & Hertz, H. M. High-resolution short-exposure small-animal laboratory x-ray phase-contrast tomography. *Scientific Reports* **6**, 39074, doi:10.1038/srep39074 (2016).

54 Benjamin, H., Jack, K., Martin, G., Ronald, R. & Rod, L. in *Proc.SPIE*.

55 Werdiger, F. *et al.* Quantification of muco-obstructive lung disease variability in mice via laboratory X-ray velocimetry. *Scientific Reports* **10**, 10859, doi:10.1038/s41598-020-67633-y (2020).

56 Burvall, A., Lundstrom, U., Takman, P. A. C., Larsson, D. H. & Hertz, H. M. Phase retrieval in X-ray phase-contrast imaging suitable for tomography. *Optics Express* **19**, 10359-10376, doi:10.1364/oe.19.010359 (2011).

57 Lohse, L. M. *et al.* A phase-retrieval toolbox for X-ray holography and tomography. *Journal of Synchrotron Radiation* **27**, 852-859, doi:doi:10.1107/S1600577520002398 (2020).

58 Chapman, D. *et al.* Diffraction enhanced x-ray imaging. *Physics in Medicine and Biology* **42**, 2015-2025, doi:10.1088/0031-9155/42/11/001 (1997).

59 Munro, P. R. T., Hagen, C. K., Szafraniec, M. B. & Olivo, A. A simplified approach to quantitative coded aperture X-ray phase imaging. *Optics Express* **21**, 11187-11201, doi:10.1364/oe.21.011187 (2013).

60 Chen, H. *et al.* Quantitative phase retrieval in X-ray Zernike phase contrast microscopy. *Journal of Synchrotron Radiation* **22**, 1056-1061, doi:doi:10.1107/S1600577515007699 (2015).

61 Paganin, D., Mayo, S. C., Gureyev, T. E., Miller, P. R. & Wilkins, S. W. Simultaneous phase and amplitude extraction from a single defocused image of a homogeneous object. *J. Microscopy* **206**, 33-40 (2002).

62 Radon, J. H. Über die Bestimmung von Funktionen durch ihre Integralwerte längs gewisser Mannigfaltigkeiten. *Ber. vor Sächs. Akad. Wiss.* **69**, 262 (1917).

63 Ramachandran, G. N. & Lakshminarayanan, A. V. Three-dimensional Reconstruction from Radiographs and Electron Micrographs: Application of Convolutions instead of Fourier Transforms. *Proceedings of the National Academy of Sciences* **68**, 2236-2240, doi:10.1073/pnas.68.9.2236 (1971).

64 Kak, A. C. & Slaney, M. *Principles of Computerized Tomographic Imaging*. (SIAM (Soc. Industrial Appl. Math.), 2001).

65 Kim, S. & Khambampati, A. K. 12 - *Mathematical concepts for image reconstruction in tomography*.in *Industrial Tomography* (ed Mi Wang) 305-346 (Woodhead Publishing, 2015).

66 Natterer, F. *The Mathematics of Computerized Tomography*. (Society for Industrial and Applied Mathematics, 2001).

67 Feldkamp, L. A., Davis, L. C. & Kress, J. W. Practical cone-beam algorithm. *Journal of the Optical Society of America a-Optics Image Science and Vision* **1**, 612-619, doi:10.1364/josaa.1.000612 (1984).

68 Katsevich, A. Theoretically Exact Filtered Backprojection-Type Inversion Algorithm for Spiral CT. *SIAM Journal on Applied Mathematics* **62**, 2012-2026, doi:10.1137/S0036139901387186 (2002).

69 Bracewell, R. N. & Riddle, A. C. Inversion of fan-beam scans in radio astronomy. *Astrophys. J.* **150**, 427-434 (1967).

70 Crowther, R. A., DeRosier, D. J. & Klug, A. The reconstruction of a three-dimensional structure from projections and its application to electron microscopy. *Proceedings of the Royal Society of London. A. Mathematical and Physical Sciences* **317**, 319-340, doi:doi:10.1098/rspa.1970.0119 (1970).

71 Rattey, P. & Lindgren, A. Sampling the 2-D Radon transform. *IEEE Transactions on Acoustics, Speech, and Signal Processing* **29**, 994-1002, doi:10.1109/TASSP.1981.1163686 (1981).

72 Beister, M., Kolditz, D. & Kalender, W. A. Iterative reconstruction methods in X-ray CT. *Physica Medica: European Journal of Medical Physics* **28**, 94-108, doi:10.1016/j.ejmp.2012.01.003 (2012).

73 Mohan, K. A. *et al.* TIMBIR: A Method for Time-Space Reconstruction From Interlaced Views. *IEEE Transactions on Computational Imaging* **1**, 96-111, doi:10.1109/tci.2015.2431913 (2015).

74 Flenner, S. *et al.* Pushing the temporal resolution in absorption and Zernike phase contrast nanotomography: enabling fast *in situ* experiments. *Journal of Synchrotron Radiation* **27**, 1339-1346, doi:doi:10.1107/S1600577520007407 (2020).

75 Park, J. *et al.* Computed tomography super-resolution using deep convolutional neural network. *Physics in Medicine & Biology* **63**, 145011, doi:10.1088/1361-6560/aacdd4 (2018).

76 Hubbell, J. H. & Seltzer, S. M. in *NIST Standard Reference Database 126* Vol. NISTIR 5632 (NIST, 2014).

77 Kinney, J. H. *et al.* Nondestructive investigation of damage in composites using x-ray tomographic microscopy. *J Mater Res* **5**, 1123-1129 (1990).

78 Dowker, S. E. P., Elliott, J. C., Davis, G. R., Wilson, R. M. & Cloetens, P. Synchrotron x-ray microtomographic investigation of mineral concentrations at micrometre scale in sound and carious enamel. *Caries Research* **38**, 514-522, doi:10.1159/000080580 (2004).

79 Donnelly, E. Methods for Assessing Bone Quality: A Review. *Clinical Orthopaedics and Related Research* **469**, 2128-2138, doi:10.1007/s11999-010-1702-0 (2011).

80 Martinez-Carvajal, G. D., Oxarango, L., Adrien, J., Molle, P. & Forquet, N. Assessment of X-ray Computed Tomography to characterize filtering media from Vertical Flow Treatment Wetlands at the pore scale. *Science of The Total Environment* **658**, 178-188, doi:<https://doi.org/10.1016/j.scitotenv.2018.12.119> (2019).

81 Heinzl, C., Amirkhanov, A. & Kastner, J. *Processing, Analysis and Visualization of CT Data.in Industrial X-ray Computed Tomography* (eds S Carmignato, W Dewulf, & R Leach) 99-142 (Springer, 2018).

82 Sezgin, M. & Sankur, B. Survey over image thresholding techniques and quantitative performance evaluation. *J Electronic Imaging* **13**, 146-168 (2004).

83 Limaye, A. in *Developments in X-Ray Tomography VIII*. (ed Stuart R. Stock) (SPIE).

84 Lee, S. B. *et al.* Pore geometry in woven fiber structures: 0°/90° plain-weave cloth lay-up preform. *J Mater Res* **13**, 1209-1217 (1998).

85 Lambert, J. *et al.* Extraction of relevant physical parameters from 3D images of foams obtained by x-ray tomography. *Colloids Surf A* **263**, 295-302. (2005).

86 Litjens, G. *et al.* A survey on deep learning in medical image analysis. *Medical image analysis* **42**, 60-88, doi:10.1016/j.media.2017.07.005 (2017).

87 Gualda, G. A. R. & Rivers, M. Quantitative 3D petrography using x-ray tomography: Application to Bishop Tuff pumice clasts. *Journal of Volcanology and Geothermal Research* **154**, 48-62, doi:<https://doi.org/10.1016/j.jvolgeores.2005.09.019> (2006).

88 Akhter, M. P., Lappe, J. M., Davies, K. M. & Recker, R. R. Transmenopausal changes in the trabecular bone structure. *Bone* **41**, 111-116, doi:10.1016/j.bone.2007.03.019 (2007).

89 Bonse, U. *et al.* in *ESRF Newsletter* Vol. March 21-23 (1996).

90 Hildebrand, T. & Ruegsegger, P. A new method for the model-independent assessment of thickness in three-dimensional images. *Journal of Microscopy* **185**, 67-75, doi:10.1046/j.1365-2818.1997.1340694.x (1997).

91 Doube, M. *et al.* BoneJ: Free and extensible bone image analysis in ImageJ. *Bone* **47**, 1076-1079, doi:<https://doi.org/10.1016/j.bone.2010.08.023> (2010).

92 Sonnemans, L. J. P., Kubat, B., Prokop, M. & Klein, W. M. Can virtual autopsy with postmortem CT improve clinical diagnosis of cause of death? A retrospective observational cohort study in a Dutch tertiary referral centre. *BMJ open* **8**, e018834, doi:10.1136/bmjopen-2017-018834 (2018).

93 Garvin, H. M. & Stock, M. K. The Utility of Advanced Imaging in Forensic Anthropology. *Academic forensic pathology* **6**, 499-516, doi:10.23907/2016.050 (2016).

94 Digital Morphology Group. *Digimorph*, <digimorph.org> (

95 Matsuda, N. *Visualizing an ancient mummy with x-ray imaging and augmented reality.in Portrait of a Child: Historical and Scientific Studies of a Roman Egyptian Mummy* (eds E Ronkko, T Terpstra, & M. Walton) 100-106 (Block Museum of Art, Northwestern University, 2019).

96 García-Moreno, F. *et al.* Using X-ray tomoscopy to explore the dynamics of foaming metal. *Nature Communications* **10**, 3762, doi:10.1038/s41467-019-11521-1 (2019).

97 Finegan, D. P. *et al.* Quantifying Bulk Electrode Strain and Material Displacement within Lithium Batteries via High-Speed Operando Tomography and Digital Volume Correlation. *Advanced Science* **3**, 1500332, doi:10.1002/advs.201500332 (2016).

98 Wang, J., Chen-Wiegart, Y.-C. K. & Wang, J. In Situ Three-Dimensional Synchrotron X-Ray Nanotomography of the (De)lithiation Processes in Tin Anodes. *Angewandte Chemie International Edition* **53**, 4460-4464, doi:10.1002/anie.201310402 (2014).

99 Leonard, F., Stein, J., Soutis, C. & Withers, P. J. The quantification of impact damage distribution in composite laminates by analysis of X-ray computed tomograms. *Composites Science and Technology* **152**, 139-148, doi:10.1016/j.compscitech.2017.08.034 (2017).

100 Bradley, R. S., Robinson, I. K. & Yusuf, M. 3D X-Ray Nanotomography of Cells Grown on
Electrospun Scaffolds. *Macromol Biosci* **17**, doi:10.1002/mabi.201600236 (2017).

101 Bultreys, T. *et al.* Fast laboratory-based micro-computed tomography for pore-scale
research: Illustrative experiments and perspectives on the future. *Advances in Water
Resources* **95**, 341-351, doi:<https://doi.org/10.1016/j.advwatres.2015.05.012> (2016).

102 Villarraga-Gómez, H., Herazo, E. L. & Smith, S. T. X-ray computed tomography: from medical
imaging to dimensional metrology. *Precision Engineering* **60**, 544-569 (2019).

103 De Chiffre, L., Carmignato, S., Kruth, J. P., Schmitt, R. & Weckenmann, A. Industrial
applications of computed tomography. *CIRP Annals* **63**, 655-677,
doi:<https://doi.org/10.1016/j.cirp.2014.05.011> (2014).

104 Warnett, J. M. *et al.* Towards in-process x-ray CT for dimensional metrology. *Measurement
Science and Technology* **27**, 35401 (2016).

105 Bauer, W., Bessler, F. T., Zabler, E. & Bergmann, R. B. in *Proc. SPIE*. (SPIE).

106 Nicoletto, G., Anzelotti, G. & Konečná, R. X-ray computed tomography vs. metallography for
pore sizing and fatigue of cast Al-alloys. *Procedia Engineering* **2**, 547-554,
doi:<https://doi.org/10.1016/j.proeng.2010.03.059> (2010).

107 Leach, R. & Carmignato, S. *Precision Metal Additive Manufacturing*. (CRC Press, 2020).

108 Sanaei, N. & Fatemi, A. Defects in Additive Manufactured Metals and Their Effect on Fatigue
Performance: A State-of-the-Art Review. *Progress in Materials Science*, 100724,
doi:<https://doi.org/10.1016/j.pmatsci.2020.100724> (2020).

109 du Plessis, A., Yadroitsev, I., Yadroitsava, I. & Le Roux, S. G. X-Ray Microcomputed
Tomography in Additive Manufacturing: A Review of the Current Technology and
Applications. *3D Printing and Additive Manufacturing* **5**, 227-247,
doi:10.1089/3dp.2018.0060 (2018).

110 Garcea, S. C., Wang, Y. & Withers, P. J. X-ray computed tomography of polymer composites.
Composites Science and Technology **156**, 305-319, doi:10.1016/j.compscitech.2017.10.023
(2018).

111 Pietsch, P. & Wood, V. X-Ray Tomography for Lithium Ion Battery Research: A Practical
Guide. *Annual Review of Materials Research* **47**, 451-479, doi:10.1146/annurev-matsci-
070616-123957 (2017).

112 Tammas-Williams, S., Withers, P. J., Todd, I. & Prangnell, P. B. Porosity regrowth during heat
treatment of hot isostatically pressed additively manufactured titanium components. *Scripta
Materialia* **122**, 72-76, doi:<http://dx.doi.org/10.1016/j.scriptamat.2016.05.002> (2016).

113 du Plessis, A. & Macdonald, E. Hot isostatic pressing in metal additive manufacturing: X-ray
tomography reveals details of pore closure. *Additive Manufacturing* **34**, 101191,
doi:<https://doi.org/10.1016/j.addma.2020.101191> (2020).

114 Tammas-Williams, S., Withers, P. J., Todd, I. & Prangnell, P. B. The Influence of Porosity on
Fatigue Crack Initiation in Additively Manufactured Titanium Components. *Scientific Reports*
7, 7308, doi:10.1038/s41598-017-06504-5 (2017).

115 Obaton, A. F. *et al.* In vivo XCT bone characterization of lattice structured implants fabricated
by additive manufacturing. *Helijon* **3**, e00374,
doi:<https://doi.org/10.1016/j.heliyon.2017.e00374> (2017).

116 Bureau International des Poids et Mesures Joint Committee for Guides in Metrology.
International vocabulary of metrology - Basic and general concepts and associated terms
(VIM). (International Organisation for Standardisation, Geneva, 2012).

117 Carmignato, S. Accuracy of industrial computed tomography measurements: Experimental
results from an international comparison. *CIRP Annals* **61**, 491-494,
doi:<https://doi.org/10.1016/j.cirp.2012.03.021> (2012).

118 Bartscher, M. *et al.* *Qualification and Testing of CT Systems in Industrial X-ray Computed
Tomography* (eds S Carmignato, W Dewulf, & R Leach) 185-228 (Springer, 2018).

119 Buratti, A., Bredeman, J., Pavan, M., Schmitt, R. & Carmignato, S. *Applications of CT for Dimensional Metrology*.in *Industrial X-ray Computed Tomography* (eds S Carmignato, W Dewulf, & R Leach) 333-369 (Springer, 2018).

120 Torralba, M., Jiménez, R., Yagüe-Fabra, J. A., Ontiveros, S. & Tosello, G. Comparison of surface extraction techniques performance in computed tomography for 3D complex micro-geometry dimensional measurements. *The International Journal of Advanced Manufacturing Technology* **97**, 441-453, doi:10.1007/s00170-018-1950-9 (2018).

121 DeHoff, R. T. & Rhine, F. N. *Quantitative Metallography*. (McGraw-Hill, 1968).

122 Asghar, Z., Requena, G. & Boller, E. Three-dimensional rigid multiphase networks providing high-temperature strength to cast AlSi10Cu5Ni1-2 piston alloys. *Acta Materialia* **59**, 6420-6432, doi:10.1016/j.actamat.2011.07.006 (2011).

123 Atwood, R. C., Jones, J. R., Lee, P. D. & Hench, L. L. Analysis of pore interconnectivity in bioactive glass foams using X-ray microtomography. *Scripta Materialia* **51**, 1029-1033, doi:10.1016/j.scriptamat.2004.08.014 (2004).

124 Maire, E. X-Ray Tomography Applied to the Characterization of Highly Porous Materials. *Annual Review of Materials Research* **42**, 163-178, doi:10.1146/annurev-matsci-070511-155106 (2012).

125 Burnett, T. L. *et al.* Correlative Tomography. *Sci. Rep.* **4**, 4177, doi:10.1038/srep04711 (2014).

126 Terzi, S., Salvo, L., Suéry, M., Dahle, A. K. & Boller, E. Internal melting and coarsening of liquid droplets in an Al–Cu alloy: a 4-D experimental study. *Journal of Materials Science* **48**, 7422-7434, doi:10.1007/s10853-013-7557-5 (2013).

127 Adrien, J., Meille, S., Tadier, S., Maire, E. & Sasaki, L. In-situ X-ray tomographic monitoring of gypsum plaster setting. *Cement and Concrete Research* **82**, 107-116, doi:<https://doi.org/10.1016/j.cemconres.2015.12.011> (2016).

128 Martin, C. F. *et al.* Characterisation by X-ray Micro-tomography of Cavity Coalescence during Superplastic Deformation. *Scripta Mater.* **42**, 375-381 (2000).

129 Lhuissier, P. *et al.* In situ 3D X-ray microtomography of laser-based powder-bed fusion (L-PBF)—A feasibility study. *Additive Manufacturing* **34**, 101271, doi:<https://doi.org/10.1016/j.addma.2020.101271> (2020).

130 Gibbs, J. W. *et al.* The Three-Dimensional Morphology of Growing Dendrites. *Scientific Reports* **5**, 11824, doi:10.1038/srep11824 (2015).

131 Maire, E., Carmona, V., Courbon, J. & Ludwig, W. Fast X-ray tomography and acoustic emission study of damage in metals during continuous tensile tests. *Acta Materialia* **55**, 6806-6815, doi:10.1016/j.actamat.2007.08.043 (2007).

132 Khor, K. H. *et al.* In situ high resolution synchrotron x-ray tomography of fatigue crack closure micromechanisms. *Journal of Physics-Condensed Matter* **16**, S3511-S3515, doi:10.1088/0953-8984/16/33/012 (2004).

133 Buffiere, J. Y., Savelli, S., Jouneau, P. H., Maire, E. & Fougeres, R. Experimental study of porosity and its relation to fatigue mechanisms of model Al-Si7-Mg0.3 cast Al alloys. *Materials Science and Engineering a-Structural Materials Properties Microstructure and Processing* **316**, 115-126 (2001).

134 Toda, H. *et al.* Quantitative assessment of microstructure and its effects on compression behavior of aluminum foams via high-resolution synchrotron X-ray tomography. *Metallurgical and Materials Transactions a-Physical Metallurgy and Materials Science* **37A**, 1211-1219, doi:10.1007/s11661-006-1072-0 (2006).

135 Mostafavi, M. *et al.* Yield behavior beneath hardness indentations in ductile metals, measured by three-dimensional computed X-ray tomography and digital volume correlation. *Acta Materialia* **82**, 468-482, doi:<https://doi.org/10.1016/j.actamat.2014.08.046> (2015).

136 Lachambre, J., Maire, E., Adrien, J. & Choqueuse, D. In situ observation of syntactic foams under hydrostatic pressure using X-ray tomography. *Acta Materialia* **61**, 4035-4043, doi:<https://doi.org/10.1016/j.actamat.2013.03.017> (2013).

137 King, A., Johnson, G., Engelberg, D., Ludwig, W. & Marrow, J. Observations of intergranular stress corrosion cracking in a grain-mapped polycrystal. *Science* **321**, 382-385, doi:10.1126/science.1156211 (2008).

138 Bale, H. A. *et al.* Real-Time Quantitative Imaging of Failure Events in Materials under Load at Temperatures above 1700°C. *Nature Materials* (2012).

139 Deville, S. *et al.* Metastable and unstable cellular solidification of colloidal suspensions. *Nature Materials* **8**, 966-972, doi:10.1038/nmat2571 (2009).

140 Ebner, M., Marone, F., Stampanoni, M. & Wood, V. Visualization and Quantification of Electrochemical and Mechanical Degradation in Li Ion Batteries. *Science* **342**, 716-720, doi:10.1126/science.1241882 (2013).

141 Finegan, D. P. *et al.* Thermal Runaway: Identifying the Cause of Rupture of Li-Ion Batteries during Thermal Runaway (Adv. Sci. 1/2018). *Advanced Science* **5**, 1870003, doi:10.1002/advs.201870003 (2018).

142 Ulrich, D., van Rietbergen, B., Weinans, H. & Ruegsegger, P. Finite element analysis of trabecular bone structure: a comparison of image-based meshing techniques. *Journal of Biomechanics* **31**, 1187-1192, doi:10.1016/s0021-9290(98)00118-3 (1998).

143 Olmos, L., Martin, C. L., Bouvard, D., Bellet, D. & Di Michiel, M. Investigation of the Sintering of Heterogeneous Powder Systems by Synchrotron Microtomography and Discrete Element Simulation. *Journal of the American Ceramic Society* **92**, 1492-1499, doi:10.1111/j.1551-2916.2009.03037.x (2009).

144 Lebensohn, R. A., Rollett, A. D. & Suquet, P. Fast fourier transform-based modeling for the determination of micromechanical fields in polycrystals. *JOM* **63**, 13-18, doi:10.1007/s11837-011-0037-y (2011).

145 Sencu, R. M., Yang, Z., Wang, Y. C., Withers, P. J. & Soutis, C. Multiscale image-based modelling of damage and fracture in carbon fibre reinforced polymer composites. *Composites Science and Technology* **198**, 108243, doi:<https://doi.org/10.1016/j.compscitech.2020.108243> (2020).

146 Müller, R. *et al.* Morphometric Analysis of Human Bone Biopsies: A Quantitative Structural Comparison of Histological Sections and Micro-Computed Tomography. *Bone* **23**, 59-66, doi:[https://doi.org/10.1016/S8756-3282\(98\)00068-4](https://doi.org/10.1016/S8756-3282(98)00068-4) (1998).

147 Obata, Y. *et al.* Quantitative and qualitative bone imaging: A review of synchrotron radiation microtomography analysis in bone research. *Journal of the Mechanical Behavior of Biomedical Materials*, 103887, doi:<https://doi.org/10.1016/j.jmbbm.2020.103887> (2020).

148 Metscher, B. D. MicroCT for comparative morphology: simple staining methods allow high-contrast 3D imaging of diverse non-mineralized animal tissues. *BMC Physiology* **9**, 11, doi:10.1186/1472-6793-9-11 (2009).

149 Koç, M. M., Aslan, N., Kao, A. P. & Barber, A. H. Evaluation of X-ray tomography contrast agents: A review of production, protocols, and biological applications. *Microscopy Research and Technique* **82**, 812-848, doi:10.1002/jemt.23225 (2019).

150 Bjork, L. & Bjorkholm, P. J. Xenon as a contrast agent for imaging of the airways and lungs using digital radiography. *Radiology* **144**, 475-478, doi:10.1148/radiology.144.3.7048416 (1982).

151 Badea, C. T. *Small Animal X-ray Computed Tomography*.in *Handbook of X-ray Imaging Physics and Technology* (ed Paolo Russo) Ch. 36, 749-774 (CRC Press, 2018).

152 Cnudde, V. *et al.* Virtual histology by means of high-resolution X-ray CT. *Journal of Microscopy* **232**, 476-485, doi:10.1111/j.1365-2818.2008.02142.x (2008).

153 Lombardi, C. M. *et al.* OP22.06: Postmortem micro-computed tomography (micro-CT) of small fetuses and hearts. *Ultrasound in Obstetrics & Gynecology* **44**, 132-133, doi:10.1002/uog.13851 (2014).

154 Hutchinson, J. C. *et al.* Clinical utility of postmortem microcomputed tomography of the fetal heart: diagnostic imaging vs macroscopic dissection. *Ultrasound in Obstetrics & Gynecology* **47**, 58-64, doi:10.1002/uog.15764 (2016).

155 Töpperwien, M. *et al.* Three-dimensional mouse brain cytoarchitecture revealed by laboratory-based x-ray phase-contrast tomography. *Scientific reports* **7**, 42847 (2017). <<https://doi.org/10.1038/srep42847>>.

156 Massimi, L. *et al.* *Laboratory-based x-ray phase contrast CT technology for clinical intra-operative specimen imaging*. Vol. 10948 MI (SPIE, 2019).

157 Ding, Y. *et al.* Computational 3D histological phenotyping of whole zebrafish by X-ray histotomography. *eLife* **8**, e44898, doi:10.7554/eLife.44898 (2019).

158 Dhondt, S., Vanhaeren, H., Van Loo, D., Cnudde, V. & Inzé, D. Plant structure visualization by high-resolution X-ray computed tomography. *Trends in Plant Science* **15**, 419-422, doi:10.1016/j.tplants.2010.05.002 (2010).

159 Rawson, S. D., Maksimcuka, J., Withers, P. J. & Cartmell, S. H. X-ray computed tomography in life sciences. *BMC Biology* **18**, 21, doi:10.1186/s12915-020-0753-2 (2020).

160 Broeckhoven, C. & du Plessis, A. X-ray microtomography in herpetological research: a review. *Amphibia-Reptilia* **39**, 377-401, doi:10.1163/15685381-20181102 (2018).

161 Faulwetter, S., Vasileiadou, A., Kouratoras, M., Dailianis, T. & Arvanitidis, C. Micro-computed tomography: Introducing new dimensions to taxonomy. *ZooKeys* **263**, 1-45 (2013).

162 Broeckhoven, C., du Plessis, A., le Roux, S. G., Mouton, P. L. N. & Hui, C. Beauty is more than skin deep: a non-invasive protocol for invivo anatomical study using micro-CT. *Methods in Ecology and Evolution* **8**, 358-369, doi:10.1111/2041-210x.12661 (2017).

163 du Plessis, A. & Broeckhoven, C. Looking deep into nature: A review of micro-computed tomography in biomimicry. *Acta Biomaterialia* **85**, 27-40, doi:10.1016/j.actbio.2018.12.014 (2019).

164 Schoeman, L., Williams, P., du Plessis, A. & Manley, M. X-ray micro-computed tomography (μ CT) for non-destructive characterisation of food microstructure. *Trends in Food Science & Technology* **47**, 10-24, doi:<https://doi.org/10.1016/j.tifs.2015.10.016> (2016).

165 Ghodki, B. M., Dadlani, G., Ghodki, D. M. & Chakraborty, S. Functional whole wheat breads: Compelling internal architecture. *LWT* **108**, 301-309, doi:<https://doi.org/10.1016/j.lwt.2019.03.066> (2019).

166 Donis-González, I. R., Guyer, D. E., Pease, A. & Barthel, F. Internal characterisation of fresh agricultural products using traditional and ultrafast electron beam X-ray computed tomography imaging. *Biosystems Engineering* **117**, 104-113, doi:<https://doi.org/10.1016/j.biosystemseng.2013.07.002> (2014).

167 Kotwaliwale, N. *et al.* X-ray imaging methods for internal quality evaluation of agricultural produce. *Journal of Food Science and Technology* **51**, 1-15, doi:10.1007/s13197-011-0485-y (2014).

168 Herremans, E. *et al.* Spatial development of transport structures in apple (*Malus × domestica* Borkh.) fruit. *Frontiers in Plant Science* **6**, doi:10.3389/fpls.2015.00679 (2015).

169 Retta, M. A., Verlinden, B., Verboven, P. & Nicolaï, B. 1256 edn 169-178 (International Society for Horticultural Science (ISHS), Leuven, Belgium).

170 Vicent, V., Ndoye, F.-T., Verboven, P., Nicolaï, B. & Alvarez, G. Effect of dynamic storage temperatures on the microstructure of frozen carrot imaged using X-ray micro-CT. *Journal of Food Engineering* **246**, 232-241, doi:<https://doi.org/10.1016/j.jfoodeng.2018.11.015> (2019).

171 Racicot, R. Fossil secrets revealed: X-Ray CT scanning and applications in paleontology. *The Paleontological Society Papers* **22**, 21-38, doi:10.1017/scs.2017.6 (2017).

172 Dunlop, J. A. *et al.* A minute fossil phoretic mite recovered by phase-contrast X-ray computed tomography. *Biology Letters* **8**, 457-460, doi:10.1098/rsbl.2011.0923 (2012).

173 Soriano, C. *et al.* Synchrotron X-ray imaging of inclusions in amber. *Comptes Rendus Palevol* **9**, 361-368, doi:<https://doi.org/10.1016/j.crpv.2010.07.014> (2010).

174 Immel, A. *et al.* Effect of X-ray irradiation on ancient DNA in sub-fossil bones – Guidelines for safe X-ray imaging. *Scientific Reports* **6**, 32969, doi:10.1038/srep32969 (2016).

175 Manning, P. L. *et al.* Biomechanics of Dromaeosaurid Dinosaur Claws: Application of X-Ray Microtomography, Nanoindentation, and Finite Element Analysis. *Anatomical Record-Advances in Integrative Anatomy and Evolutionary Biology* **292**, 1397-1405, doi:10.1002/ar.20986 (2009).

176 Grimaldi, D. *Insects from the Santana Formation, Lower Cretaceous, of Brazil*. Vol. 195 (1990).

177 Martill, D. M., Bechly, G. & Loveridge, R. F. *The Crato Fossil Beds of Brazil: Window into an Ancient World*. (Cambridge University Press, 2007).

178 van de Kamp, T. *et al.* Parasitoid biology preserved in mineralized fossils. *Nature communications* **9**, 3325 (2018). <<https://europepmc.org/articles/PMC6113268>>.

179 Schwermann, A. H. *et al.* Preservation of three-dimensional anatomy in phosphatized fossil arthropods enriches evolutionary inference. *eLife* **5**, e12129, doi:10.7554/eLife.12129 (2016).

180 Grimaldi, D. & Engel., M. S. *Evolution of the Insects*. (Cambridge University Press, 2005).

181 Grimaldi, D., Bonwich, E., Delannoy, M. & Doberstein, S. Electron microscopic studies of mummified tissues in amber fossils. *American Museum Novitates* **3097**, 1-31 (1994).

182 Henderickx, H. *et al.* Description of a new fossil Pseudogarypus (Pseudoscorpiones : Pseudogarypidae) with the use of X-ray micro-CT to penetrate opaque amber. *Zootaxa*, 41-50, doi:10.11646/zootaxa.1305.1.4 (2006).

183 Langenheim, J. H. *Plant resins: chemistry, evolution, ecology, and ethnobotany*. (Timber Press, 2003).

184 Anderson, K. B. *The Nature and Fate of Natural Resins in the Geosphere. V. New Evidence Concerning the Structure, Composition and Maturation of Class I (Polylabdanoid) Resinates*.in *ACS Symposium Series* Vol. 617 (eds Ken B. Anderson & John C. Crelling) 105-129 (1995).

185 Grimaldi, D. A. & Ross, A. *Extraordinary Lagerstätten in amber, with particular reference to the Cretaceous of Burma*.in *Terrestrial Conservation Lagerstätten, Windows into the Evolution of Life on Land* (eds N.C Fraser & H.-D. Sues) 287-342 (Dunedin Press, 2017).

186 Clarke, D. J., Limaye, A., McKenna, D. D. & Oberprieler, R. G. The Weevil Fauna Preserved in Burmese Amber-Snapshot of a Unique, Extinct Lineage (Coleoptera: Curculionoidea). *Diversity* **11**, 1 (2019).

187 Stankiewicz, B. A., Poinar, H. N., Briggs, D. E. G., Evershed, R. P. & Poinar, G. O. Chemical preservation of plants and insects in natural resins. *Proc Biol Sci* **265**, 641-647, doi:10.1098/rspb.1998.0342 (1998).

188 Sherratt, E. *et al.* Amber fossils demonstrate deep-time stability of Caribbean lizard communities. *Proceedings of the National Academy of Sciences* **112**, 9961-9966, doi:10.1073/pnas.1506516112 (2015).

189 Daza, J. D., Stanley, E. L., Wagner, P., Bauer, A. M. & Grimaldi, D. A. Mid-Cretaceous amber fossils illuminate the past diversity of tropical lizards. *Science Advances* **2**, e1501080, doi:10.1126/sciadv.1501080 (2016).

190 Schlüter, S., Sammartino, S. & Koestel, J. Exploring the relationship between soil structure and soil functions via pore-scale imaging. *Geoderma* **370**, 114370, doi:<https://doi.org/10.1016/j.geoderma.2020.114370> (2020).

191 Menon, M. *et al.* Pore system characteristics of soil aggregates and their relevance to aggregate stability. *Geoderma* **366**, 114259, doi:<https://doi.org/10.1016/j.geoderma.2020.114259> (2020).

192 Diel, J., Vogel, H.-J. & Schlüter, S. Impact of wetting and drying cycles on soil structure dynamics. *Geoderma* **345**, 63-71, doi:<https://doi.org/10.1016/j.geoderma.2019.03.018> (2019).

193 Hanna, R. D. & Ketcham, R. A. X-ray computed tomography of planetary materials: A primer and review of recent studies. *Geochemistry* **77**, 547-572, doi:<https://doi.org/10.1016/j.chemer.2017.01.006> (2017).

194 Rassouli, F. S., Ross, C. M., Zoback, M. D. & Andrew, M. in *51st U.S. Rock Mechanics/Geomechanics Symposium* 16 (American Rock Mechanics Association, San Francisco, California, USA, 2017).

195 Cnudde, V. *et al.* Multi-disciplinary characterisation of a sandstone surface crust. *Science of The Total Environment* **407**, 5417-5427, doi:<https://doi.org/10.1016/j.scitotenv.2009.06.040> (2009).

196 Cnudde, V. *et al.* High-resolution X-ray CT for 3D petrography of ferruginous sandstone for an investigation of building stone decay. *Microscopy Research and Technique* **74**, 1006-1017, doi:10.1002/jemt.20987 (2011).

197 Cnudde, V. *et al.* 3D characterization of sandstone by means of X-ray computed tomography. *Geosphere* **7**, 54-61, doi:10.1130/ges00563.1 (2011).

198 Boone, M. *et al.* Three-dimensional phase separation and identification in granite. *Geosphere* **7**, 79-86, doi:10.1130/ges00562.1 (2011).

199 Laforce, B. *et al.* Integrated Three-Dimensional Microanalysis Combining X-Ray Microtomography and X-Ray Fluorescence Methodologies. *Anal Chem* **89**, 10617-10624, doi:10.1021/acs.analchem.7b03205 (2017).

200 Pankhurst, M. J., Gueninchault, N., Andrew, M. & Hill, E. Non-destructive three-dimensional crystallographic orientation analysis of olivine using laboratory diffraction contrast tomography. *Mineralogical Magazine* **83**, 705-711, doi:10.1180/mgm.2019.51 (2019).

201 Prodanović, M., Mehmani, A. & Sheppard, A. P. Imaged-based multiscale network modelling of microporosity in carbonates. *Geological Society, London, Special Publications* **406**, 95, doi:10.1144/SP406.9 (2015).

202 Polacci, M. *et al.* Crystallisation in basaltic magmas revealed via in situ 4D synchrotron X-ray microtomography. *Scientific Reports* **8**, 8377, doi:10.1038/s41598-018-26644-6 (2018).

203 Pistone, M., Caricchi, L., Fife, J. L., Mader, K. & Ulmer, P. In situ X-ray tomographic microscopy observations of vesiculation of bubble-free and bubble-bearing magmas. *Bulletin of Volcanology* **77**, 108, doi:10.1007/s00445-015-0992-1 (2015).

204 Wadsworth, F. B. *et al.* A general model for welding of ash particles in volcanic systems validated using in situ X-ray tomography. *Earth and Planetary Science Letters* **525**, 115726, doi:<https://doi.org/10.1016/j.epsl.2019.115726> (2019).

205 Oughanem, R. *et al.* A Multi-Scale Investigation of Pore Structure Impact on the Mobilization of Trapped Oil by Surfactant Injection. *Transport in Porous Media* **109**, 673-692, doi:10.1007/s11242-015-0542-5 (2015).

206 Zhang, G. *et al.* Effects of uniaxial and triaxial compression tests on the frozen sandstone combining with CT scanning. *International Journal of Physical Modelling in Geotechnics* **19**, 261-274, doi:10.1680/jphmg.18.00006 (2019).

207 Lenoir, N., Bornert, M., Desrues, J., Besuelle, P. & Viggiani, G. Volumetric digital image correlation applied to X-ray microtomography images from triaxial compression tests on argillaceous rock. *Strain* **43**, 193-205 (2007).

208 Ketcham, R. A. Computational methods for quantitative analysis of three-dimensional features in geological specimens. *Geosphere* **1**, 32-41, doi:10.1130/ges00001.1 (2005).

209 Sheppard, A. P., Sok, R. M. & Averdunk, H. Techniques for image enhancement and segmentation of tomographic images of porous materials. *Physica A: Statistical Mechanics and its Applications* **339**, 145-151 (2004).

210 Vlassenbroeck, J. *et al.* Software tools for quantification of X-ray microtomography at the UGCT. *Nuclear Instruments and Methods in Physics Research Section A: Accelerators, Spectrometers, Detectors and Associated Equipment* **580**, 442-445, doi:<https://doi.org/10.1016/j.nima.2007.05.073> (2007).

211 Andrew, M. A quantified study of segmentation techniques on synthetic geological XRM and FIB-SEM images. *Computational Geosciences* **22**, 1503-1512, doi:10.1007/s10596-018-9768-y (2018).

212 Weckenmann, A. *et al.* Multisensor data fusion in dimensional metrology. *CIRP Annals* **58**, 701-721, doi:<https://doi.org/10.1016/j.cirp.2009.09.008> (2009).

213 Verein Deutscher Ingenieure e.V. Computed tomography in dimensional measurement - Fundamentals and definitions. (Dusseldorf, 2018).

214 Verein Deutscher Ingenieure e.V. Computed tomography in dimensional measurement - Influencing variables on measurement results and recommendations for computed tomography dimensional measurements. (Dusseldorf, 2018).

215 ASTM. Standard Test Method for Measurement of Computed Tomography (CT) System Performance. (ASTM International, West Conshohocken, PA, 2020).

216 ASTM. ASTM E1441-19, Standard Guide for Computed Tomography (CT). (ASTM International, West Conshohocken, PA, 2020).

217 Ferrucci, M., Leach, R. K., Giusca, C., Carmignato, S. & Dewulf, W. Towards geometrical calibration of x-ray computed tomography systems—a review. *Measurement Science and Technology* **26**, 092003, doi:10.1088/0957-0233/26/9/092003 (2015).

218 Dewulf, W. *et al.* Enhanced dimensional measurement by fast determination and compensation of geometrical misalignments of X-ray computed tomography instruments. *CIRP Annals* **67**, 523-526, doi:<https://doi.org/10.1016/j.cirp.2018.04.124> (2018).

219 Verein Deutscher Ingenieure e.V. Computed tomography in dimensional measurement - Determination of the uncertainty of measurement and test process suitability of coordinate measurements systems with CT sensors. (Dusseldorf, 2015).

220 Ferrucci, M. *Towards Traceability of CT Dimensional Measurements*.in *Industrial X-ray Computed Tomography* (eds S Carmignato, W Dewulf, & R Leach) 229-266 (Springer, 2018).

221 Angel, J. & De Chiffre, L. Comparison on Computed Tomography using industrial items. *CIRP Annals* **63**, 473-476, doi:<https://doi.org/10.1016/j.cirp.2014.03.034> (2014).

222 Bartscher, M., Illemann, J. & Neuschaefer-Rube, U. ISO test survey on material influence in dimensional computed tomography. *Case Studies in Nondestructive Testing and Evaluation* **6**, 79-92, doi:<https://doi.org/10.1016/j.csndt.2016.04.001> (2016).

223 Verein Deutscher Ingenieure e.V. Accuracy of coordinate measuring machines - Characteristics and their testing - Guideline for the application of DIN EN ISO 10360 for coordinate measuring machines with CT-sensors. (Dusseldorf, 2011).

224 Illemann, J. *et al.* Procedure and reference standard to determine the structural resolution in coordinate metrology. *Measurement Science and Technology* **25**, 064015, doi:10.1088/0957-0233/25/6/064015 (2014).

225 Zanini, F. & Carmignato, S. Two-spheres method for evaluating the metrological structural resolution in dimensional computed tomography. *Measurement Science and Technology* **28**, 114002, doi:10.1088/1361-6501/aa85b7 (2017).

226 Sokac, M. *et al.* Improved surface extraction of multi-material components for single-source industrial X-ray computed tomography. *Measurement* **153**, 107438, doi:<https://doi.org/10.1016/j.measurement.2019.107438> (2020).

227 Wallander, H. & Wallentin, J. Simulated sample heating from a nanofocused X-ray beam. *Journal of Synchrotron Radiation* **24**, 925-933, doi:doi:10.1107/S1600577517008712 (2017).

228 Schneider, G. Cryo X-ray microscopy with high spatial resolution in amplitude and phase contrast. *Ultramicroscopy* **75**, 85-104, doi:[https://doi.org/10.1016/S0304-3991\(98\)00054-0](https://doi.org/10.1016/S0304-3991(98)00054-0) (1998).

229 Reisz, J. A., Bansal, N., Qian, J., Zhao, W. & Furdui, C. M. Effects of ionizing radiation on biological molecules--mechanisms of damage and emerging methods of detection. *Antioxid Redox Signal* **21**, 260-292, doi:10.1089/ars.2013.5489 (2014).

230 Meganck, J. A. & Liu, B. Dosimetry in Micro-computed Tomography: a Review of the Measurement Methods, Impacts, and Characterization of the Quantum GX Imaging System. *Mol Imaging Biol* **19**, 499-511, doi:10.1007/s11307-016-1026-x (2017).

231 Waarsing, J. H. *et al.* Detecting and tracking local changes in the tibiae of individual rats: a novel method to analyse longitudinal *in vivo* micro-CT data. *Bone* **34**, 163-169, doi:<https://doi.org/10.1016/j.bone.2003.08.012> (2004).

232 Zhao, Y. *et al.* High-resolution, low-dose phase contrast X-ray tomography for 3D diagnosis of human breast cancers. *Proceedings of the National Academy of Sciences*, 201204460, doi:10.1073/pnas.1204460109 (2012).

233 Tavakoli Taba, S. *et al.* Propagation-Based Phase-Contrast CT of the Breast Demonstrates Higher Quality Than Conventional Absorption-Based CT Even at Lower Radiation Dose. *Academic Radiology*, doi:10.1016/j.acra.2020.01.009.

234 Raupach, R. & Flohr, T. G. Analytical evaluation of the signal and noise propagation in x-ray differential phase-contrast computed tomography. *Physics in Medicine and Biology* **56**, 2219-2244, doi:10.1088/0031-9155/56/7/020 (2011).

235 Kitchen, M. J. *et al.* CT dose reduction factors in the thousands using X-ray phase contrast. *Scientific Reports* **7**, 15953, doi:10.1038/s41598-017-16264-x (2017).

236 Davis, G. R. & Elliott, J. C. X-ray microtomography scanner using time-delay integration for elimination of ring artefacts in the reconstructed image. *Nucl. Instr. Meth A* **394**, 157-162 (1997).

237 Davis, G. R. & Elliott, J. C. Artefacts in X-ray microtomography of materials. *Mat. Sci. & Tech.* **22** 1011-1018 (2006).

238 Nardi, C. *et al.* Metal and motion artifacts by cone beam computed tomography (CBCT) in dental and maxillofacial study. *La radiologia medica* **120**, 618-626, doi:10.1007/s11547-015-0496-2 (2015).

239 Kastner, J. & Heinzl, C. *X-Ray Tomography*.in *Handbook of Advanced Non-Destructive Evaluation* (eds Nathan Ida & Norbert Meyendorf) 1-72 (Springer International Publishing, 2018).

240 Kyrieleis, A., Ibison, M., Titarenko, V. & Withers, P. J. Image stitching strategies for tomographic imaging of large objects at high resolution at synchrotron sources. *Nucl. Instr. Meth. Phys. Res. A* **607**, 677-684 (2009).

241 Barrett, J. F. & Keat, N. Artifacts in CT: Recognition and Avoidance. *Radiographics* **24**, 1679-1691, doi:10.1148/rg.246045065 (2004).

242 Xiao, X., De Carlo, F. & Stock, S. Practical error estimation in zoom-in and truncated tomography reconstructions. *Rev. Sci. Instr.* **78**, 063705 (2007).

243 Boas, F. E. & Fleischmann, D. CT artifacts: causes and reduction techniques. *Imaging in Medicine* **4** (2012).

244 Kyrieleis, A., Titarenko, V., Ibison, M., Connelly, T. & Withers, P. J. Region-of-interest tomography using filtered backprojection: assessing the practical limits. *J. Microsc.* **241**, 69-82, doi:10.1111/j.1365-2818.2010.03408.x (2011).

245 Yun, W. *et al.* Novel, High Brightness X-ray Source and High Efficiency X-ray Optic for Development of X-ray Instrumentation. *Microscopy and Microanalysis* **22**, 118-119, doi:10.1017/S1431927616001446 (2016).

246 Gruse, J. N. *et al.* Application of compact laser-driven accelerator X-ray sources for industrial imaging. *Nuclear Instruments and Methods in Physics Research Section A: Accelerators, Spectrometers, Detectors and Associated Equipment* **983**, 164369, doi:<https://doi.org/10.1016/j.nima.2020.164369> (2020).

247 Martín-Vega, D., Simonsen, T. J., Wicklein, M. & Hall, M. J. R. Age estimation during the blow fly intra-puparial period: a qualitative and quantitative approach using micro-computed tomography. *Int J Legal Med* **131**, 1429-1448, doi:10.1007/s00414-017-1598-2 (2017).

248 Leth, P. M. The use of CT scanning in forensic autopsy. *Forensic Science, Medicine, and Pathology* **3**, 65-69, doi:10.1385/FSMP:3:1:65 (2007).

249 Thompson, W. M., Lionheart, W. R. B., Morton, E. J., Cunningham, M. & Luggar, R. D. High speed imaging of dynamic processes with a switched source x-ray CT system. *Measurement Science & Technology* **26**, doi:10.1088/0957-0233/26/5/055401 (2015).

250 Jailin, C., Buljac, A., Bouterf, A., Hild, F. & Roux, S. Fast four-dimensional tensile test monitored via X-ray computed tomography: Elastoplastic identification from radiographs. *The Journal of Strain Analysis for Engineering Design* **54**, 44-53, doi:10.1177/0309324718810593 (2019).

251 Vavrik, D., Jakubek, J., Kumpova, I. & Pichotka, M. Dual energy CT inspection of a carbon fibre reinforced plastic composite combined with metal components. *Case Studies in Nondestructive Testing and Evaluation* **6**, 47-55, doi:<https://doi.org/10.1016/j.csndt.2016.05.001> (2016).

252 Egan, C. K. *et al.* 3D chemical imaging in the laboratory by hyperspectral X-ray computed tomography. *Scientific Reports* **5**, 15979, doi:10.1038/srep15979 (2015).

253 Sittner, J. *et al.* Spectral X-ray computed micro tomography: 3-dimensional chemical imaging. *X-Ray Spectrometry* **n/a**, doi:<https://doi.org/10.1002/xrs.3200> (2020).

254 Poulsen, H. F. *et al.* Three-dimensional maps of grain boundaries and the stress state of individual grains in polycrystals and powders. *Journal of Applied Crystallography* **34**, 751-756, doi:10.1107/s0021889801014273 (2001).

255 Larson, B. C., W. Yang, G.E. Ice, Budai, J. D. & Tischler, J. Z. Three-dimensional X-ray structural microscopy with submicrometre resolution. *Nature* **415**, 887-890 (2002).

256 Johnson, G., King, A., Honnicke, M. G., Marrow, J. & Ludwig, W. X-ray diffraction contrast tomography: a novel technique for three-dimensional grain mapping of polycrystals. II. The combined case. *Journal of Applied Crystallography* **41**, 310-318, doi:10.1107/s0021889808001726 (2008).

257 Frølich, S. *et al.* Diffraction tomography and Rietveld refinement of a hydroxyapatite bone phantom. *Journal of Applied Crystallography* **49**, 103-109, doi:10.1107/S1600576715022633 (2016).

258 Birkbak, M. E. *et al.* Concurrent determination of nanocrystal shape and amorphous phases in complex materials by diffraction scattering computed tomography. *Journal of Applied Crystallography* **50**, 192-197, doi:10.1107/S1600576716019543 (2017).

259 Egan, C. K. *et al.* Dark-field hyperspectral X-ray imaging. *Proceedings of the Royal Society a-Mathematical Physical and Engineering Sciences* **470**, 20130629, doi:10.1098/Rspa.2013.0629 (2014).

260 Kagias, M., Wang, Z., Jefimovs, K. & Stampanoni, M. Dual phase grating interferometer for tunable dark-field sensitivity. *Applied Physics Letters* **110**, 014105, doi:10.1063/1.4973520 (2017).

261 De Boever, W. *et al.* Characterization of composition and structure of clay minerals in sandstone with ptychographic X-ray nanotomography. *Applied Clay Science* **118**, 258-264, doi:10.1016/j.clay.2015.09.020 (2015).

262 Burnett, T. L. & Withers, P. J. Completing the picture through correlative characterization. *Nature Materials* **18**, 1041-1049, doi:10.1038/s41563-019-0402-8 (2019).

263 Starborg, T. *et al.* Experimental steering of electron microscopy studies using prior X-ray computed tomography. *Ultramicroscopy* **201**, 58-67, doi:<https://doi.org/10.1016/j.ultramic.2019.03.002> (2019).

264 Dunlop, J. A. *et al.* Computed tomography recovers data from historical amber: an example from huntsman spiders. *Naturwissenschaften* **98**, 519-527, doi:10.1007/s00114-011-0796-x (2011).

265 Maire, E., Le Bourlot, C., Adrien, J., Mortensen, A. & Mokso, R. 20 Hz X-ray tomography
during an in situ tensile test. *International Journal of Fracture* **200**, 3-12,
doi:10.1007/s10704-016-0077-y (2016).

266 Walker, S. M. *et al.* In Vivo Time-Resolved Microtomography Reveals the Mechanics of the
Blowfly Flight Motor. *PLOS Biology* **12**, e1001823, doi:10.1371/journal.pbio.1001823 (2014).

267 Bultreys, T. *et al.* Real-time visualization of Haines jumps in sandstone with laboratory-based
microcomputed tomography. *Water Resources Research* **51**, 8668-8676,
doi:10.1002/2015WR017502 (2015).

268 Bay, B. K., Smith, T. S., Fyhrie, D. P. & Saad, M. Digital volume correlation: Three-dimensional
strain mapping using X-ray tomography. *Experimental Mechanics* **39**, 217-226 (1999).

269 Roux, S., Hild, F., Viot, P. & Bernard, D. Three-dimensional image correlation from X-ray
computed tomography of solid foam. *Composites Part a-Applied Science and Manufacturing*
39, 1253-1265, doi:10.1016/j.compositesa.2007.11.011 (2008).

270 Kobayashi, M. *et al.* High-density three-dimensional mapping of internal strain by tracking
microstructural features. *Acta Materialia* **56**, 2167-2181, doi:10.1016/j.actamat.2007.12.058
(2008).

271 Toda, H., Maire, E., Aoki, Y. & Kobayashi, M. Three-dimensional strain mapping using in situ
X-ray synchrotron microtomography. *Journal of Strain Analysis for Engineering Design* **46**,
549-561, doi:10.1177/0309324711408975 (2011).